AGU PUBLICATIONS

JGR

Journal of Geophysical Research: Solid Earth

RESEARCH ARTICLE
10.1002/2015JB012303

**Key Points:**
- $^{26}$Al-$^{10}$Be isochron burial ages and lidar data constrain bedrock incision rates
- Incision rates spanning ~2.9 Myr imply differential rock uplift over two folds
- Modest uplift and shortening imply that other regional structures are also active

**Supporting Information:**
- Texts S1–S3, Tables S1 and S2, and Figures S1–S12

**Correspondence to:**
A. M. Bender,
abender@usgs.gov

**Citation:**
Bender, A. M., C. B. Amos, P. Bierman, D. H. Rood, L. Staisch, H. Kelsey, and B. Sherrod (2016), Differential uplift and incision of the Yakima River terraces, central Washington State, *J. Geophys. Res. Solid Earth*, *121*, 365–384, doi:10.1002/2015JB012303.

Received 28 JUN 2015
Accepted 4 DEC 2015
Accepted article online 9 DEC 2015
Published online 16 JAN 2016



# Differential uplift and incision of the Yakima River terraces, central Washington State

**Adrian M. Bender[1], Colin B. Amos[1], Paul Bierman[2], Dylan H. Rood[3,4], Lydia Staisch[5], Harvey Kelsey[6], and Brian Sherrod[5]**

[1]Geology Department, Western Washington University, Bellingham, Washington, USA, [2]Department of Geology and Rubenstein School of the Environment and Natural Resources, University of Vermont, Burlington, Vermont, USA, [3]Department of Earth Science and Engineering, Imperial College London, London, UK, [4]Scottish Universities Environmental Research Centre, East Kilbride, UK, [5]U.S. Geological Survey Earthquake Science Center, Department of Earth and Space Sciences, University of Washington, Seattle, Washington, USA, [6]Geology Department, Humboldt State University, Arcata, California, USA

**Abstract** The fault-related Yakima folds deform Miocene basalts and younger deposits of the Columbia Plateau in central Washington State. Geodesy implies ~2 mm/yr of NNE directed shortening across the folds, but until now the distribution and rates of Quaternary deformation among individual structures has been unclear. South of Ellensburg, Washington, the Yakima River cuts a ~600 m deep canyon across several Yakima folds, preserving gravel-mantled strath terraces that record progressive bedrock incision and related rock uplift. Here we integrate cosmogenic isochron burial dating of the strath terrace gravels with lidar analysis and field mapping to quantify rates of Quaternary differential incision and rock uplift across two folds transected by the Yakima River: Manastash and Umtanum Ridge. Isochron burial ages from in situ produced $^{26}$Al and $^{10}$Be at seven sites across the folds date episodes of strath terrace formation over the past ~2.9 Ma. Average bedrock incision rates across the Manastash (~88 m/Myr) and Umtanum Ridge (~46 m/Myr) anticlines are roughly 4 to 8 times higher than rates in the intervening syncline (~14 m/Myr) and outside the canyon (~10 m/Myr). These contrasting rates demonstrate differential bedrock incision driven by ongoing Quaternary rock uplift across the folds at rates corresponding to ~0.13 and ~0.06 mm/yr shortening across postulated master faults dipping 30 ± 10°S beneath the Manastash and Umtanum Ridge anticlines, respectively. The reported Quaternary shortening across the anticlines accounts for ~10% of the ~2 mm/yr geodetic budget, suggesting that other Yakima structures actively accommodate the remaining contemporary deformation.

## 1. Introduction

A comprehensive understanding of upper plate deformation along active convergent margins requires measurements of the deformation spanning $10^0$ to $10^6$ year intervals and over spatial scales sufficient to capture the influence of key tectonic structures. Relatively few areas have complete spatial and temporal records of deformation, however, resulting in knowledge gaps that pose critical issues for regional seismic hazard analyses [e.g., *Petersen et al.*, 2014]. The Cascadia convergent margin in the U.S. Pacific Northwest represents a locale where geodesy quantifies crustal strain far inboard of the subduction zone over several decades (Figure 1 inset), but concomitant rates of geologic strain at $10^2$–$10^6$ year intervals lack equivalent spatial coverage [*McCaffrey et al.*, 2013]. Upper plate deformation along the Cascadia margin incorporates oblique Pacific-North American plate motion, along with basin and range extension, resulting in clockwise rotation of the western Oregon fore arc and consequent shortening on both sides of the Cascade volcanic arc in Washington (Figure 1) [*McCaffrey et al.*, 2013; *Wells and McCaffrey*, 2013; *Wells et al.*, 1998]. East-west and northwest striking fore arc faults between northwestern Oregon and Washington record Quaternary to Holocene reverse faulting [*Blakely et al.*, 2002; *Johnson et al.*, 1999, 1996; *Kelsey et al.*, 2012, 2008; *Nelson et al.*, 2003; *Sherrod et al.*, 2013, 2008, 2004] cumulatively accounting for most of the ~5 mm/yr of geodetically observed regional shortening [*McCaffrey et al.*, 2013]. Geodesy indicates that the rate of contemporary N-S shortening diminishes to ~2 mm/yr east of the Cascade arc, where fault-related folds developed in the Miocene Columbia River Basalts —the Yakima folds (Figure 1)—appear to accommodate the deformation. The rates of shortening distributed among specific Yakima fold structures remain unknown [*McCaffrey et al.*, 2013].

Geologic evidence for recent tectonic deformation among the Yakima folds is limited. Paleoseismic investigations of tectonic scarps, offset landforms, and faulted stratigraphy reveal evidence for late Pleistocene to Holocene activity on several Yakima folds, but rates remain poorly constrained [*Blakely et al.*, 2011;

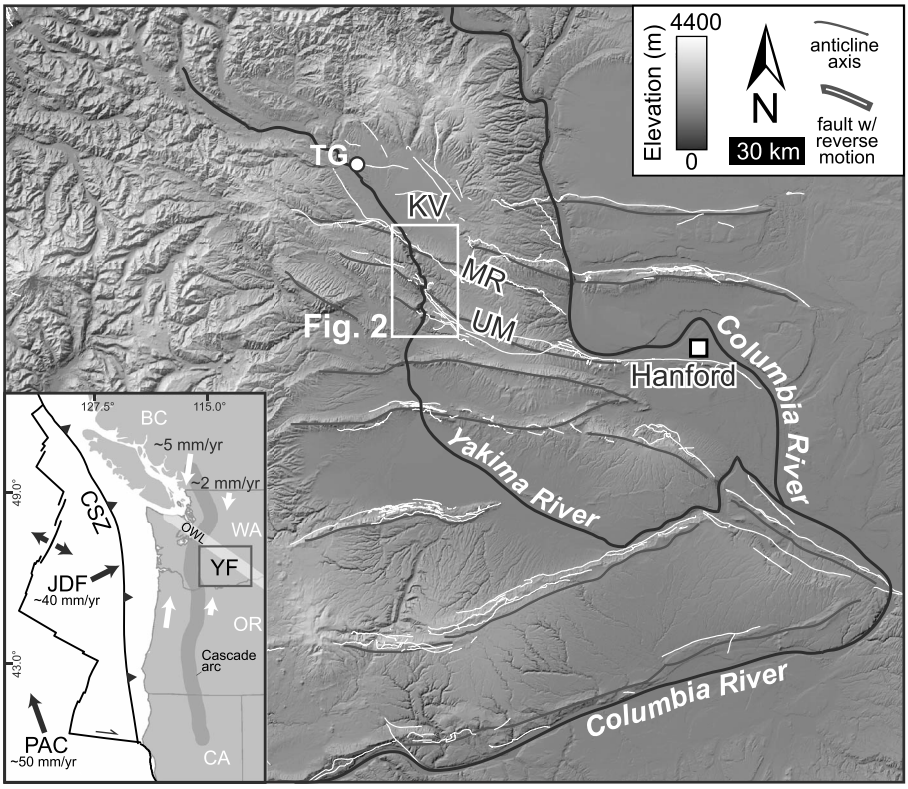


**Figure 1.** Structural and topographic map of the Yakima folds in central Washington. Map depicts study area in the Yakima River Canyon across Manastash (MR) and Umtanum Ridge (UR) structures south of Kittitas Valley (KV) and west of the Hanford Nuclear Reservation. Thin dark grey lines represent anticline axes, white lines represent known or suspected Quaternary active faults with reverse motion from Washington Department of Natural Resources (http://www.dnr.wa.gov/ResearchScience/Topics/GeosciencesData/Pages/gis_data.aspx). Thorp Gravel (TG) fission track age and type location from Figure 2 in *Waitt* [1979]. Inset shows the relationship between the Pacific plate (PAC), Juan de Fuca plate (JDF), Cascadia subduction zone (CSZ), Yakima folds (YF) and faults [e.g., *Wells et al.*, 1998], and the Olympic-Wallowa Lineament (OWL) [*Raisz*, 1945]. Inset also depicts contemporary NNE shortening across the Cascade fore arc and back arc regions implied by geodesy—for GPS station locations and geodetic analysis see Figures 9–10 and related text in *McCaffrey et al.* [2013].

*Campbell and Bentley*, 1981; *Ladinsky*, 2012; *Reidel*, 1984; *West et al.*, 1996]. Erosion during repeated late Pleistocene Lake Missoula flooding [*Bretz*, 1969; *Waitt*, 1980, 1985] limited the preservation of landforms and deposits that recorded earlier Quaternary deformation in low-lying areas. The importance of establishing Quaternary geochronologic constraints on the Yakima folds is twofold. First, knowing geologic deformation rates establishes the relative contribution of Quaternary folding and faulting to the full tectonic development of the Yakima folds and the Cascade back arc. For example, some researchers postulate that the structural development of the Yakima folds and faults occurred entirely between 10.5 and ~2.9 Ma [e.g., *Reidel*, 1984], but the lack of geochronologic constraints on younger deformation leaves this assertion untested. Second, while geodesy demonstrates ~2 mm/yr of shortening across the Yakima folds over the past ~20 years [*McCaffrey et al.*, 2013], it remains unclear which structures accommodate this surface deformation at what rate and over what interval. This uncertainty represents a significant gap in the current assessment of Pacific Northwest seismic hazards, especially given the $\geq M_w 7$ seismic potential of the ~200 km long Yakima fold belt faults near the Hanford nuclear site (Figure 1) [*Wells and Coppersmith*, 1994; *Blakely et al.*, 2011].

This study focuses on the Yakima River Canyon, located south of the Kittitas Valley, Washington (Figure 1). Here the Yakima River incises a meandering canyon up to ~600 m deep and nearly perpendicular to strike across three of the Yakima folds: Manastash Ridge, Umtanum Ridge, and Selah Butte, from north to south (Figure 2a). The presence of minimally incised alluvium-filled basins upstream (Kittitas Valley) and downstream (Selah Valley) of the deep basalt canyon suggests that canyon incision is a direct response to fold-related rock uplift. The canyon contains a suite of predominately unpaired strath terraces that consist

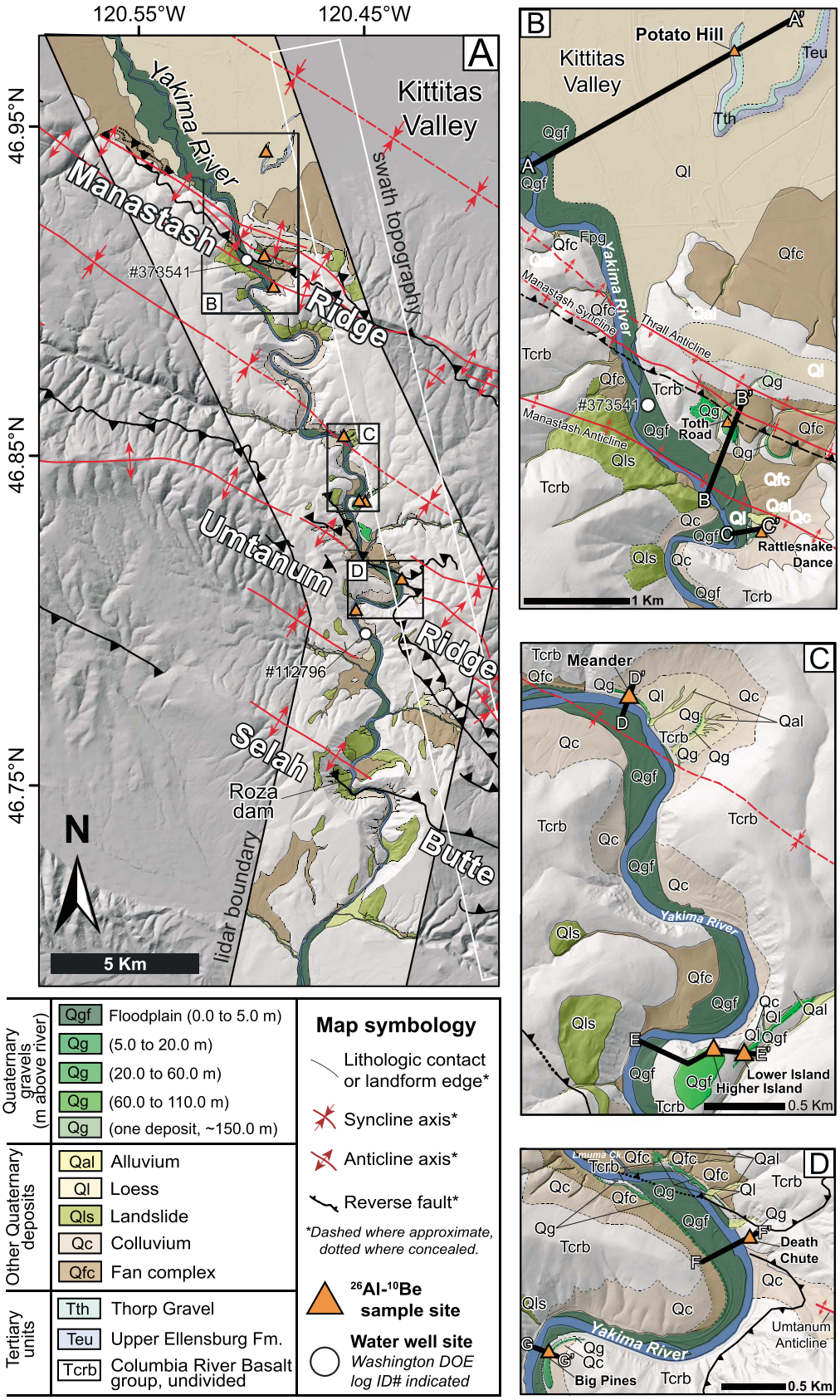
120.55°W
120.45°W
46.95°N
46.85°N
46.75°N
A
Kittitas Valley
Yakima River
Manastash Ridge
swath topography
#373541
B
C
Umtanum Ridge
D
#112796
Selah
Roza dam
Butte
lidar boundary
N
5 Km
B
Potato Hill
A'
Teu
Tth
Qgf
Ql
Qfc
Fpg
Yakima River
Manastash Syncline
Thrall Anticline
Tcrb
Qg
B'
Toth Road
Manastash Anticline
Qls
Qal
Qc
C'
Rattlesnake Dance
1 Km
C
Meander
D'
Lower Island
Higher Island
0.5 Km
D
Death Chute
F'
Umtanum Anticline
G'
Big Pines
0.5 Km
Quaternary gravels (m above river)
Qgf Floodplain (0.0 to 5.0 m)
Qg (5.0 to 20.0 m)
Qg (20.0 to 60.0 m)
Qg (60.0 to 110.0 m)
Qg (one deposit, ~150.0 m)
Other Quaternary deposits
Qal Alluvium
Ql Loess
Qls Landslide
Qc Colluvium
Qfc Fan complex
Tertiary units
Tth Thorp Gravel
Teu Upper Ellensburg Fm.
Tcrb Columbia River Basalt group, undivided
Map symbology
Lithologic contact or landform edge*
Syncline axis*
Anticline axis*
Reverse fault*
*Dashed where approximate, dotted where concealed.
26Al-10Be sample site
Water well site
Washington DOE log ID# indicated

**Figure 2**

of both local (basaltic) and Cascade Range-derived gravels (mixed rock type) overlying the beveled basalt straths. In this paper, we use "strath" to reference the beveled basaltic bedrock surface overlain by the river gravels and "strath terrace" to describe landforms that comprise a strath, capping gravel, and related cover deposits.

Our investigation of the Yakima River terraces builds on mapping by *Ladinsky* [2012] and *Coppersmith et al*. [2014] and on initial cosmogenic isotope data presented in *Coppersmith et al*. [2014]. We use the $^{26}$Al-$^{10}$Be isochron burial dating method [*Balco and Rovey*, 2008; *Çiner et al*., 2015; *Erlanger et al*., 2012; *Darling et al*., 2014] to analyze quartz-bearing clasts in the terrace gravels and estimate the age of the terraces. We use lidar and field observations to map the strath terraces and constrain strath elevations. At each dated strath we estimate cumulative incision relative to the active bedrock channel and use the cosmogenic ages to determine local bedrock incision rates. We also calculate local bedrock incision rates using the method of *Gallen et al*. [2015] to address the potential for incision rate bias [*Finnegan et al*., 2014] introduced by the transient active channel elevation and compare results between the two different approaches. We subtract the background rate of downcutting within and outside the canyon to estimate the rate of differential bedrock incision driven by uplift and deformation of the Yakima folds [e.g., *Lavé and Avouac*, 2001; *Pazzaglia and Brandon*, 2001; *Wegmann and Pazzaglia*, 2002]. Relating the vertical rock uplift rates to horizontal shortening across the Manastash and Umtanum Ridge anticlines provides the first quantitative estimate of late Quaternary deformation rates across these structures. Our assessment reveals the relative contribution of the Manastash and Umtanum structures to the total modern shortening budget and clarifies the potential seismic hazard of faults related to the Yakima folds.

## 2. Location and Geologic Framework

The Yakima folds form a structural province of the western Columbia Plateau in south central Washington and north central Oregon (Figure 1). The province comprises 14 anticlines developed in pre-Miocene crystalline and sedimentary basement rocks, Miocene flows and intercalated sediments of the Columbia River Basalt Group [e.g., *Reidel et al*., 2013], and in overlying Plio-Pleistocene fluvial and lacustrine units [e.g., *Bingham and Grolier*, 1966; *Waitt*, 1979; *Campbell and Bentley*, 1981]. Blind thrusting appears to control folding on the anticlines [e.g., *Casale and Pratt*, 2015; *Ladinsky*, 2012; *Miller*, 2014], which are primarily NNE-NNW directed and trend ENE-WNW [e.g., *Reidel*, 1984]. Regional topography mimics bedrock structure, with the folds expressed as relatively high, narrow anticlinal ridges, and broad intervening synclinal valleys. Fold wavelengths range from ~5 to 35 km (Figure 1) [*Watters*, 1988, 1989]. Individual anticlinal ridges commonly exceed 100 km in length (Figure 1) and typically consist of a gently south dipping backlimb that folds over into a steeply north dipping forelimb. Thrust faults place the forelimb of one anticline over the backlimb of the adjacent anticline to the north, thus defining the intervening synclinal valleys [e.g., *Reidel*, 1984].

Based on geophysical evidence, *Saltus* [1993] and *Pratt* [2012] suggest that initial development of the Yakima folds and faults may have started prior to the emplacement of the Columbia River Basalts. Since early descriptions and mapping of the Yakima folds by *Russell* [1893] and *Smith* [1903], workers proposed various mechanisms for their origin, including wrinkle ridges analogous to those identified on Mars [*Watters*, 1988, 1989] and splay faults related to pre-Miocene dextral shear on the Olympic-Wallowa Lineament (OWL) [*Hooper and Conrey*, 1989; *Pratt*, 2012; *Raisz*, 1945]. The OWL [*Raisz*, 1945] comprises a swath of aligned topographic features, including several Yakima folds, continuous from the Wallowa Mountains in Oregon, across the Cascade volcanic arc, to the Olympic Peninsula in Washington (Figure 1 inset). Geophysical lineaments beneath the OWL may represent structural links between the Yakima folds and Holocene active faults in the Puget Sound [*Blakely et al*., 2011, 2014], calling into question the nature and potential tectonic significance of features within and adjacent to the lineament. GPS measurements resolve contemporary shortening across the Yakima folds and the OWL [*McCaffrey et al*., 2013], and *Wells and McCaffrey* [2013] attribute the deformation to distributed strain consistent with the Cascadia margin geologic record spanning the past 16 Myr.

**Figure 2.** Quaternary geologic map of the Yakima River Canyon, depicting strath terrace gravels and cosmogenic sample sites. (a) Lettered boxes correspond to (b–d) detail maps. Lines of section in detail maps correspond to Figure 5 interpretive cross sections. Geologic mapping overlies 2008 EarthScope lidar data (accessed through www.opentopography.org). Geologic and structural mapping in area of (B) is modified from [*Ladinsky*, 2012]. Swath topography box indicates area profiled in Figures 7a and 8.

The Yakima folds and related faults record ~25 km of north-south shortening since the youngest deformed member of the Columbia River Basalts erupted at 10.5 Ma [*Reidel*, 1984]. The average north-south shortening rate since 10.5 Ma (~2.4 mm/yr) is similar to the north-northeast south-southwest geodetic rate (1.9 ± 0.5 mm/yr) integrated over ~20 years [*McCaffrey et al*., 2013]. Neither the geologic nor geodetic estimate can resolve the rate and distribution of Quaternary deformation on individual Yakima folds. However, the geodetic shortening, along with contemporary seismicity [*Blakely et al*., 2012; *Gomberg et al*., 2012; *Wicks et al*., 2011] and paleoseismic evidence [*Campbell and Bentley*, 1981; *Reidel*, 1984; *West et al*., 1996; *Blakely et al*., 2011; *Ladinsky*, 2012], collectively suggests continuing tectonic development of the Yakima folds through Quaternary time.

The Yakima River Canyon (Figure 2) provides several opportunities for characterizing Quaternary deformation within the OWL. The canyon lies beyond the farthest regional Quaternary glacial advance [*Porter*, 1976] and above inundation and scour by the Lake Missoula outburst floods [*Bretz*, 1969; *Waitt*, 1980, 1985]. The modern Yakima River generally incises <5 m into the broad Kittitas and Selah Valley floors, north and south of the bedrock canyon, respectively. Given comparatively modest incision in these bounding basins, cutting of the ~600 m deep canyon requires a significant component of differential rock uplift. The relatively uniform durability of the Miocene Columbia River Basalts flooring the canyon suggests that variations in channel substrate do not substantially affect fluvial downcutting in the canyon [e.g., *Duvall et al*., 2004]. The unpaired strath terraces and associated gravel deposits flanking Manastash and Umtanum Ridges (Figure 2) should therefore provide a relatively complete record of Quaternary bedrock incision and uplift across these structures.

## 3. Methods

### 3.1. Surficial Mapping

We mapped the surficial geology of the Yakima River Canyon using field observations and analysis of EarthScope airborne lidar data accessed through the Open Topography portal (www.opentopography.org). Our mapping builds on preliminary surficial geologic mapping by *Ladinsky* [2012] across Manastash Ridge and revises remote surface mapping through the canyon [*Coppersmith et al*., 2014, Appendix E]. We mapped the canyon between the Selah Valley to the south and Kittitas Valley to the north (Figure 2). We adopt bedrock mapping from the Washington Department of Natural Resources 1:100,000 scale geologic map database [*Schuster*, 1994; *Walsh*, 1986]. We group the Grand Ronde and Wanapum flows of the Columbia River Basalt Group, along with the comparatively thin (tens of meters thick) intervening Vantage sedimentary horizon as undivided Tertiary Columbia River Basalt Group. Using lidar derivatives (e.g., hillshades, slope maps, and contours), we mapped Quaternary landforms and deposits in the field including terraces, landslides, alluvial fans, loess, and colluvium at a scale of 1:20,000. We mapped strath terrace remnants from field observations at a scale of 1:5000 (Figure 2). Our mapping also covered Selah Butte, the southernmost of the three anticlines incised by the Yakima River Canyon (Figure 2a), but revealed no exposed strath terraces across the fold, possibly due to burial by large landslides into the canyon (Figure 2a).

Most of the strath terraces represent unpaired, isolated remnants with little downstream continuity, which prevented straightforward correlation of individual landforms based on geomorphic and geologic criteria. We did not attempt to characterize strath terraces by degree of soil development both because of limited exposure and because terrace soils were in most all cases buried by meters of loess and/or colluvium (see the supporting information file for descriptions of terrace deposits and stratigraphy). Instead, we classify mapped Quaternary gravel (Qg) deposits based on relative elevation above the river channel. The lowest unit (Qgf, 0.0–5.0 m) occupies the canyon floodplain, and the remaining four Qg units span up to ~150 m above the river.

### 3.2. $^{26}$Al-$^{10}$Be Isochron Burial Dating and Sampling

We employ the cosmogenic $^{26}$Al-$^{10}$Be isochron burial dating method [*Balco and Rovey*, 2008; *Erlanger et al*., 2012] to determine burial ages for strath-capping terrace gravels and establish bounds on the timing of terrace formation (Figure 3). The $^{26}$Al-$^{10}$Be isochron burial method provides several key advantages for dating the Yakima River terrace gravels in comparison to other Quaternary geochronology methods. First, the isochron burial method works well for deposits between ~0.2 and ~4.0 Ma [*Balco and Rovey*, 2008].

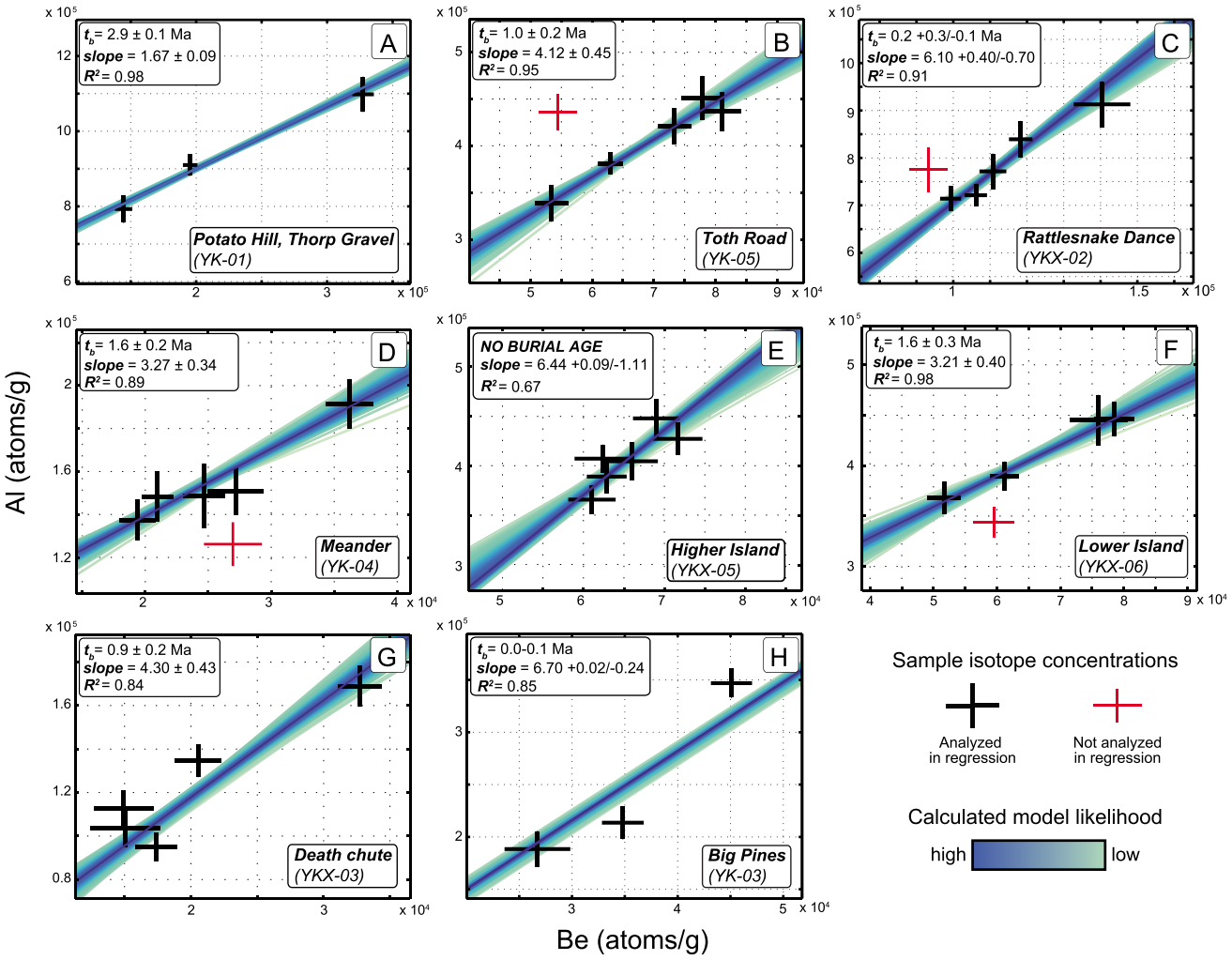


**Figure 3.** Cosmogenic $^{26}$Al-$^{10}$Be isochron plots for samples collected at each site, constructed using a Bayesian linear regression algorithm modeling the likelihood of 100,000 lines fit to the isotope data. Crosses represent 1$\sigma$ uncertainties and thin red crosses represent outliers (>2$\sigma$ from the mode line of best fit) omitted from isochron analysis. Slope and age uncertainties are based on uncertainty at the 1$\sigma$ or 68% confidence range for Gaussian and asymmetrical posterior slope distributions, respectively (see section 3 for detailed explanation).

Given the 3.64 ± 0.37 (1$\sigma$) Ma age of the highest surface incised by the Yakima River in the northern Kittitas Valley (Figure 1) [*Waitt*, 1979], we expected the terrace gravels in the canyon downstream to fall within this range. Also, terrace gravels contain quartz-bearing clasts that are distinctly exotic to the basalt-floored canyon and likely sourced in the Cascade Range. The Cascade Mountain source requires ~100 km of transport by the Yakima River (Figure 4a) and therefore permits associating the strath terrace deposits with the main Yakima River channel. Finally, the quartz in the Cascade-derived clasts allows measurement of in situ $^{26}$Al and $^{10}$Be concentrations which can be used to infer the timing of deposition in the active bedrock channel.

Like the simple, single clast cosmogenic burial dating techniques [e.g., *Granger*, 2006], the isochron method leverages a fixed ratio of in situ $^{26}$Al and $^{10}$Be production in quartz exposed at the surface, and the differential rates of isotope decay after surface production stops. Several studies demonstrate that the surface production ratio ($R_{init}$) may vary with latitude and/or altitude [*Borchers et al.*, 2015; *Lifton et al.*, 2014; *Argento et al.*, 2013]. We employ the commonly accepted [e.g., *Balco and Rovey*, 2008] $R_{init}$ value of 6.75 $^{26}$Al:$^{10}$Be atoms, which is consistent with the $R_{init}$ value calibrated in the western U.S. at Promontory Point, Utah, where the latitude and altitude are similar to the Yakima River terrace sites [*Lifton et al.*, 2015]. The decay constants $\lambda_{26}$ (9.83 ± 0.25 × $10^{-7}$ atoms/yr) and $\lambda_{10}$ (5.10 ± 0.26 × $10^{-7}$ atoms/yr) define rates of nuclide decay

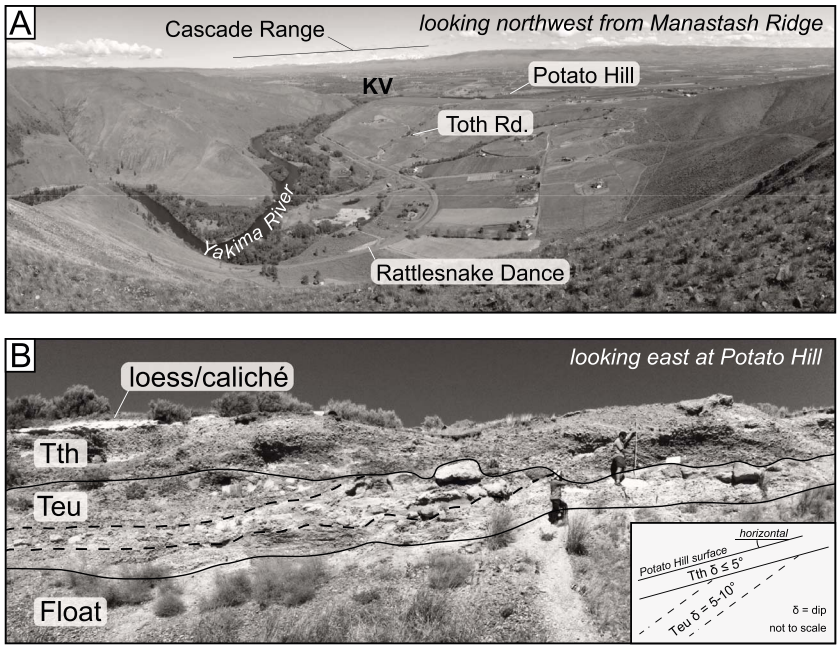


**Figure 4.** (a) View northwest from Manastash Ridge over Kittitas Valley (KV), the mouth of the Yakima River Canyon, and the Manastash Ridge sample sites. The ~100 km distant Cascade Range provides the source for the strath terrace gravels in the Yakima River Canyon. (b) Potato Hill sample site depicting stratigraphic relationships observed in the field and described by *Bentley* [1977]. Inset shows a simplified interpretation of the stratigraphy identified in the photo. Dashed lines represent internal bedding, possibly growth strata, in the Tertiary Upper Ellensburg (Teu) formation. The suspected growth strata dip 5–10° north and are truncated and capped by 2–3 m thick ~2.9 Ma Thorp Gravel dipping up to 5° north. The Potato Hill surface dips in agreement with the Thorp Gravel (Tth) and is variably capped by thick caliche under loess. The white signboard marks the cosmogenic sample location, and the stadia rod is 2 m tall.

corresponding with half-lives of 0.705 Myr for $^{26}$Al [*Nishiizumi*, 2004] and 1.36 Myr for $^{10}$Be [*Chmeleff et al*., 2010; *Nishiizumi et al*., 2007].

Unlike other cosmogenic burial dating techniques, the isochron burial method does not require information about the depth, exposure duration, or postburial nuclide production of the samples [*Balco and Rovey*, 2008]. Instead, the isochron method requires sampling clasts with a range of isotope concentrations that record varying (but unknown) preburial exposure histories but common postburial production and decay, as well as sufficient sedimentary cover (≥2 m) to minimize postburial isotope production. The method assumes that sampling clasts from the same depth horizon (≥2 m below the surface) in a given deposit fulfill the requirement of common postburial history. The methodological assumption is important for dating the Yakima terrace gravels because (1) the deposits tend to be relatively thin (≤5 m) and may therefore be susceptible to postburial nuclide production, and (2) we lack information about the preburial exposure history and thus the nuclide inheritance of the samples we collected.

The slope ($R_M$) of a line fit to measured nuclide concentrations from clasts collected at each deposit plotted as $^{10}$Be versus $^{26}$Al reflects the deviation from the surface production ratio ($R_{\text{init}}$) (Figures S1a–S1d in the supporting information). Because this deviation is dependent on isotope half-life and duration of decay, the burial age ($t_b$) is then calculated as

$$t_b = -\ln(R_M/R_{\text{init}}) \,/\, (\lambda_{26} - \lambda_{10}) \quad (1)$$

In some cases, geologic limitations inherent to the method may lead to outliers or uninterpretable results in the isochron analysis. For example, sampling from a particular depth horizon assumes that each clast entered the horizon with quartz having a $^{26}$Al/$^{10}$Be ratio of 6.75, consistent with the surface production ratio and the initial isochron slope. The assumption fails if individual clasts in the horizon underwent a previous episode of burial at depth sufficient for protection from cosmic radiation (≥2 m) over a period of time similar to or exceeding the isotope half-lives. In this case, differential radioactive decay during the previous burial episode

**Table 1.** Sample Site Data Summary

| Site Name | Site ID[a] | Latitude[b] | Longitude[b] | Strath Elevation (m)[c] | Channel Elevation (m)[c] | Sample Interval (m)[d] | Sample Height Above Strath (m) | Cumulative Bedrock Incision (m)[e] | $^{26}$Al-$^{10}$Belsochron Burial Ages (Ma)[f] | IRSL Ages (ka)[g] | Local Bedrock Incision Rate (m/Myr)[h] |
|---|---|---|---|---|---|---|---|---|---|---|---|
| Potato Hill | YK-01 | 46.9122 | −120.4954 | 437 | 415 | 2.7–3.1 | 0.0–0.3 | 28 ± 5 | 2.9 ± 0.1 | -- | 10 ± 2 |
| Toth Road | YK-05 | 46.9094 | −120.4975 | 463 | 407 | 2.1–2.3 | ~2–3 | 62 ± 5 | 1.0 ± 0.2 | -- | 61 ± 13 |
| Rattlesnake Dance | YKX-02 | 46.8999 | −120.4937 | 423 | 406 | 4.7–4.9 | ~1 | 23 ± 5 | 0.2 + 0.3/−0.1 | 84.2–93.3 | 114 + 164/−79 |
| Meander | YK-04 | 46.8539 | −120.4649 | 395 | 379 | 6.6–6.8 | 0.2–0.4 | 22 ± 5 | 1.6 ± 0.2 | -- | 14 ± 4 |
| Higher Island | YKX-05 | 46.8342 | −120.4589 | 473 | 372 | 1.7–1.9 | 0.0–0.2 | 107 ± 5 | -- | -- | -- |
| Lower Island | YKX-06 | 46.8339 | −120.4563 | 434 | 372 | 2.0–2.3 | ~1 | 62 ± 5 | 1.6 ± 0.3 | -- | 42 ± 9 |
| Death Chute | YKX-03 | 46.8090 | −120.4411 | 404 | 366 | 4.3–4.6 | 0.7–1.0 | 38 ± 5 | 0.9 ± 0.2 | -- | 49 ± 12 |
| Big Pines | YK-03 | 46.8015 | −120.4618 | 365 | 360 | 5.3–5.6 | ~2 | 5 ± 5 | 0.0–0.1 | -- | ≥66 |

[a]YK- denotes site initially sampled by *Coppersmith et al.* [2014] and resampled in this study. YKX- denotes site first mapped and sampled in this study.
[b]World Geodetic System 84 coordinates.
[c]From 2008 EarthScope lidar data set, references the ellipsoid vertical datum.
[d]Sample interval measured from top of exposure or pit.
[e]See text for discussion of calculation and nominal 5 m uncertainty.
[f]This study, cosmogenic isochron burial ages of gravel deposits, uncertainties represent 1$\sigma$ error.
[g]Ladinsky [2012], age of loess over gravel (therefore minimum limit for terrace age).
[h]1$\sigma$ Gaussian uncertainties, 68% confidence interval asymmetrical uncertainties.

results in initial $^{26}$Al/$^{10}$Be ratio of <6.75 for a clast. If true for a only a few clasts sampled in the horizon, then the samples will yield concentrations of $^{26}$Al depleted relative to $^{10}$Be and plot as outliers below the regression in the isochron analysis of the sample suite. Alternatively, if all of the material sampled in a given horizon systematically shares the same prior burial episode (unlikely in mixed, fluvially transported gravel), then isochron analysis of the samples would overestimate the burial age.

Uninterpretable results can also occur if clasts buried with inadequate sedimentary shielding from cosmic radiation (<2 m) over time periods that are equivalent to, or exceed the isotope half-lives. In this case, the postburial $^{26}$Al and $^{10}$Be production overprints the postburial decay, resulting in an isochron slope that remains indistinguishable from the surface production slope of 6.75 and yields a burial age indistinguishable from zero years. This specific case requires contextual geologic or geomorphic constraints on the deposit to determine whether the zero age is anomalous or whether the deposit may actually be younger than the lower effective limit of the isochron burial method (i.e., < 0.2 Ma).

In the more general case, where clasts are subjected to both postburial decay and production, the *y* intercept of the measured isochron estimates the amount of postburial production in the sampled depth horizon. The assumed initial isochron line passes through the origin (i.e., *y* intercept = 0); in the absence of postburial production, the relative postburial decay of $^{26}$Al and $^{10}$Be decreases the slope of the isochron without influencing the *y* intercept. The concomitant occurrence of postburial production increases the *y* intercept value of the isochron proportionally to the amount of postburial isotope production but does not change the isochron slope. In this case, the isochron analysis provides an accurate burial age as a result of the common postburial clast history and also detects the influence of the postburial isotope production in the sampled clasts.

We collected 15 quartz-bearing cobbles, plus several kilograms of sand and mixed pebbles from within a 20–30 cm thick horizon at least 2 m below the top of each strath-capping gravel deposit (Table 1). Quartz abundance determined which samples were suitable for extraction and measurement of $^{26}$Al and $^{10}$Be, so sampling 15 cobbles at each site helped to ensure that an adequate number of the clasts ($n \geq 3$) yielded quartz in sufficient amounts for analysis. We analyzed quartz from individual cobbles, amalgamated pebbles, and amalgamated sand sampled at each site. Because different individual cobbles and amalgamated grain sizes can record different preburial histories, analyzing isotope concentrations among the different grain size samples maximizes the potential range of isotope concentrations for isochron analysis. In order to ensure that the cosmogenic ages best represent the timing of terrace formation, we sampled sediment for analysis from directly above the bedrock strath whenever possible.

All samples were prepared at the University of Vermont Cosmogenic Isotope Laboratory facilities following standard lab protocols [e.g., *Corbett et al.*, 2011]. Sample $^{26}$Al/$^{27}$Al and $^{10}$Be/$^{9}$Be ratios were measured on the Scottish Universities Environmental Research Centre accelerator mass spectrometry (AMS) laboratory in

East Kilbride, Scotland [*Xu et al*., 2015]. The supporting information provides a detailed description of sample preparation, AMS measurement, and blank correction protocols.

The main sources of analytic uncertainty contributing to $^{26}$Al-$^{10}$Be isochron burial ages are errors on the nuclide decay constants (~3%) and uncertainties related to AMS measurements [*Balco and Rovey*, 2008]. Decay constant uncertainties contribute uniformly to each burial age, but measurement uncertainties vary. Hence, $^{26}$Al-$^{10}$Be isochron analyses require a linear regression technique that weighs the measurement uncertainties related to each plotted concentration. Previous $^{26}$Al-$^{10}$Be isochron burial age studies [e.g., *Balco and Rovey*, 2008; *Çiner et al*., 2015; *Darling et al*., 2014; *Erlanger et al*., 2012] use the regression method of *York* [1966] to address this issue, but we employ a Bayesian approach to linear regression developed by *D'Agostini* [2003, 2005] and first applied to $^{26}$Al-$^{10}$Be isochron burial dating isochrons by *Muzikar* [2011].

The Bayesian approach varies from the *York* [1966] method in two ways. First, rather than assuming uncorrelated slope and errors in fitting a single optimum line to data, Bayesian linear regression tests the likelihood of many slope and intercept value combinations fitting data with $x$ and $y$ errors and resolves correlation between the modeled parameters. Normalized relative probability distributions of modeled slope and intercept estimate confidence around the most likely estimate of each parameter and may or may not be Gaussian. Where the probability distributions are not Gaussian, we use the 68% confidence interval to assign asymmetrical age uncertainties. Most of the probability distributions in this study tend to be Gaussian, in which case we consider the 68% confidence interval as the 1$\sigma$ uncertainty. Second, the Bayesian method allows investigators to constrain modeled regression parameter output based on a priori geologic information. For example, the age of a gravel deposit cannot be less than zero; therefore, the slope of a line fit to an isochron plot of $^{26}$Al and $^{10}$Be concentrations cannot be greater than $R_{\mathrm{init}}$ (the slope corresponding to the surface production ratio of $^{26}$Al/$^{10}$Be, nominally 6.75). Hence, 6.75 is a suitable upper limit for modeled slope output.

We use a MATLAB script implementing Bayesian linear regression statistics to construct $^{26}$Al-$^{10}$Be burial isochrons. The script runs a Monte Carlo simulation algorithm to fit a chosen number of lines to bivariate data with associated errors within optionally specified windows of slope and intercept and calculates likelihood of fit for each line. The likelihood of each model is calculated based on the assumption that the $x$ and $y$ uncertainties for the measured data have a Gaussian distribution. Using this methodology, we test the likelihood of 100,000 linear regression models with slopes between 0 and 6.75 fit to $^{26}$Al and $^{10}$Be concentration data from each of the eight sampled terrace gravel deposits. We use the mode of the a posteriori slope values as the measured slope variable $R_M$ in equation (1) to calculate burial ages. We calculate burial age uncertainty at the 1$\sigma$ (Gaussian) or 68% confidence (asymmetrical) range from the posterior probability density functions for the regression slope and analyze each result as $R_M$ in equation (1).

On each isochron we plot all $^{26}$Al and $^{10}$Be concentration data and 1$\sigma$ uncertainties corresponding to the given site (Figure 3). We omit samples from regression analysis if the measured $^{26}$Al (and $^{10}$Be) concentrations plot greater than 2$\sigma$ away from the mode linear regression model. For samples with anomalously high $^{26}$Al concentrations (i.e., 2$\sigma$ above the line of best fit), we attribute the outliers to laboratory uncertainty [e.g., *Erlanger et al*., 2012] related to misestimation of $^{9}$Be or $^{27}$Al or error in the AMS measurement of $^{10}$Be or $^{26}$Al. For anomalously low $^{26}$Al concentrations (i.e., 2$\sigma$ below the line of best fit), we attribute the outliers to previous cycles of burial and reworking, resulting in a violation of the assumption that the initial $^{10}$Be/$^{26}$Al ratio results only from preburial surface exposure.

### 3.3. Bedrock Incision

We combine terrace gravel burial ages with lidar elevation data to calculate rates of bedrock incision at seven locations in the Yakima River Canyon. Since the gravel burial age provides a minimum age for the underlying basaltic bedrock strath, the cumulative bedrock incision divided by the burial age yields the maximum time-averaged incision rate [*Bull*, 1991; *Burbank and Anderson*, 2011; *Hancock and Anderson*, 2002]. The calculation generally relies on estimating cumulative incision by comparing the height of abandoned strath terraces with the active, bedrock channel elevation as a lower reference datum [*Pazzaglia and Brandon*, 2001; *Wegmann and Pazzaglia*, 2002]. Recent work, however, calls into question the reliability of local bedrock incision rates referencing the modern channel height [*Finnegan et al*., 2014; *Gallen et al*., 2015], given that bedrock incision and terrace formation require alternating periods of lateral erosion and aggradation and thus fluctuations in

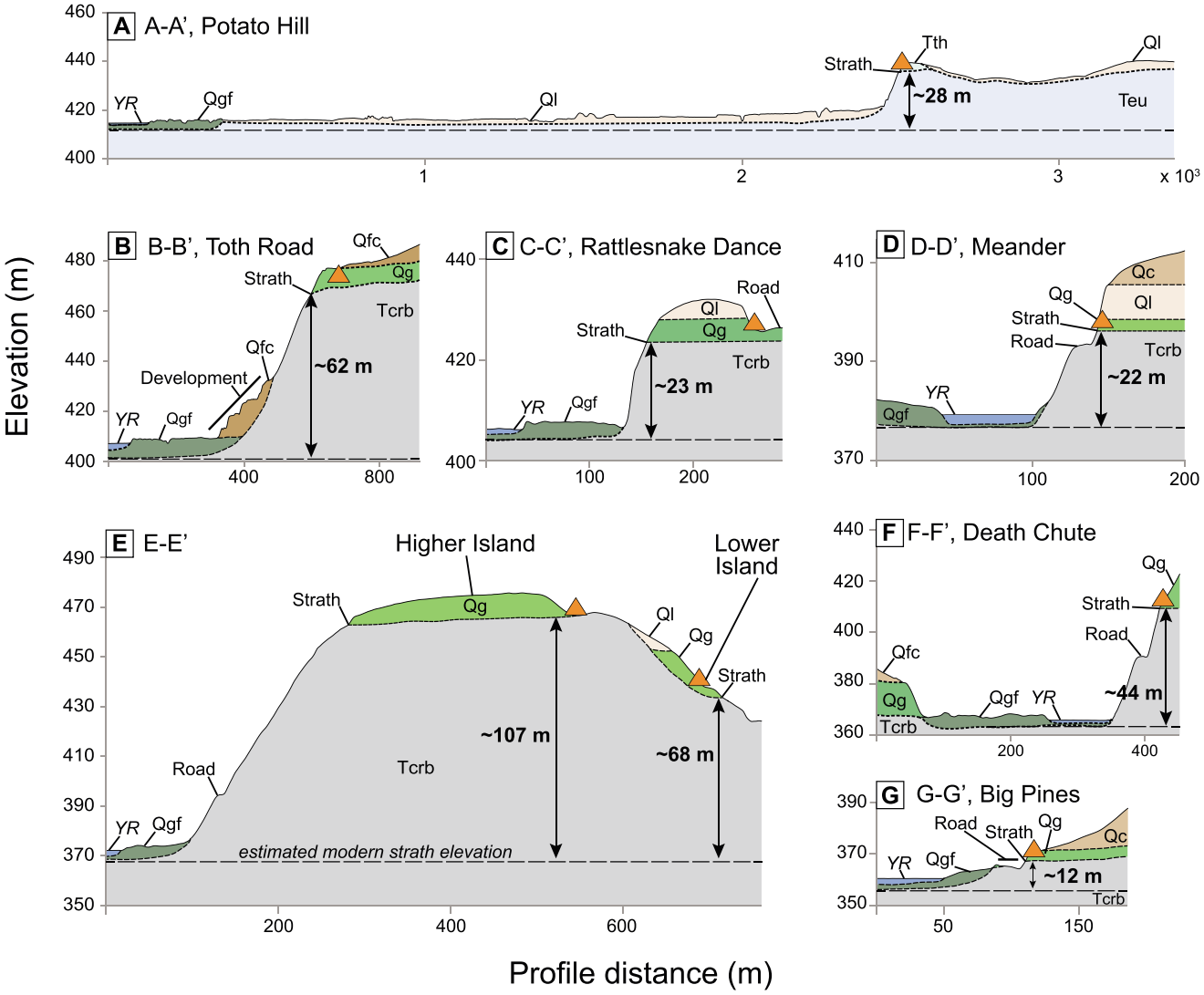


**Figure 5.** Interpretive cross sections through strath terrace sites sampled for $^{26}$Al-$^{10}$Be isochron burial dating, based on geologic mapping in Figure 2. Symbology and geologic units explained in Figure 2. Profile locations are shown by lettered lines in Figures 2b, 2c, and 2d, and topographic data are from 2008 EarthScope lidar. Arrows indicate estimated Yakima River (YR) incision into the basalt strath at each sample site.

riverbed elevation [e.g., *Bull*, 1991; *Hancock and Anderson*, 2002; *Wegmann and Pazzaglia*, 2009]. Therefore, in addition to calculating local rates of bedrock incision relative to the active bedrock channel, we also apply the method of *Gallen et al.* [2015] as an alternative approach to assess the potential influence of the transient active channel elevation.

Applying this alternative approach, we estimate cumulative local bedrock incision relative to the lowest and youngest dated strath terrace and calculate the corresponding measurement interval as the difference between gravel burial ages [*Gallen et al.*, 2015]. We regress the incision and age data referencing both datums to estimate the associated long-term average incision rates as the slope of the linear fits [e.g., *Pederson et al.*, 2006, 2013] using the same Bayesian regression method employed for the isochron burial age estimates. We incorporate a data point (0 Myr, 0 m incision) in the regressions to represent the known age and incision into bedrock beneath the active channel alluvium (i.e., the modern strath, Figures 5a–5g). Comparing the long-term average rates from each approach enables our assessment of the potential influence of the transient active channel elevation on the incision rates referencing the active channel.

The strath elevations used to estimate cumulative incision are based on point elevations of gravel-over-strath contacts beneath cosmogenic sample locations mapped on a 1.5 m vertical resolution lidar-derived digital

elevation model (DEM). The point elevations are extracted from vertical cross-channel profiles (Figures 5a–5g) at the intersection of the profile with the mapped contact and verified by field measurements of cover deposit thickness. While the exposed and mapped strath positions are well constrained, the associated point elevations may not adequately represent lateral variations in the elevation of the buried strath surface, thereby introducing uncertainty to calculations of cumulative incision. Calculating cumulative incision also requires projecting the strath elevations to either the position of the modern channel or the position of the lowest dated strath, which compounds elevation uncertainties because the point elevations are subject to similar lateral elevation variations. Finally, the active channel reference datum may or may not represent the channel position at the time that the strath being used to calculate incision was originally beveled, adding further uncertainty to estimates of cumulative incision. These implicit factors, in addition to the DEM resolution, lead us to assign a nominal uncertainty of 5 m to calculated estimates of cumulative bedrock incision.

To better estimate the amount of cumulative local bedrock incision, we also consider the thickness of modern alluvium in the active bedrock channel for local incision rates based on strath height (Table 1) above the active Yakima River channel. Throughout the canyon, we observed that the Yakima River incises ~1–2 m into floodplain alluvium, so we assume that the floodplain and active channel overlie the same strath. Drilling logs from local water wells (Washington Department of Ecology IDs 112796 and 373541, available online at https://fortress.wa.gov/ecy/waterresources/map/WCLSWebMap) suggest an average gravel thickness between of ~8 m along the floodplain within the Yakima River Canyon. Each well site (Figures 2a and 2b) is positioned ~2 m above the Yakima River water surface, so we estimate the gravel thickness beneath the modern channel at ~6 m. Hence, we offset each strath height by adding the representative 6 m to calculate local cumulative bedrock incision. We calculate incision rate uncertainty by propagating the nominal incision and $1\sigma$ burial age uncertainties in quadrature for sites with Gaussian errors and assess a range of permissible incision rates at the 68% confidence range for sites with asymmetrical uncertainty.

## 4. Yakima River Terrace Sample Sites

### 4.1. Kittitas Valley

Miocene Columbia River Basalt Group and overlying Miocene upper Ellensburg Formation volcaniclastic rocks floor the broad Kittitas Valley (Figures 1, 2a, 2b, and 4a). Pliocene Thorp Gravel caps this underlying bedrock and is discontinuously overlain by Quaternary loess of the Palouse Formation [*Porter*, 1976; *Waitt*, 1979]. *Waitt* [1979] interpreted the Thorp Gravel as outwash transported by the main stream of the ancestral Yakima River, forming the paleosurface of Kittitas Valley and reported a fission track age of $3.64 \pm 0.37$ ($1\sigma$) Ma for a tephra in the Thorp Gravel at a site 25–30 km to the northwest of Potato Hill (Figure 1) [see *Waitt*, 1979, Table 1 and Figures 1, 2, and 5]. *Bentley* [1977] correlated the uppermost gravel at Potato Hill to the Thorp type location, mapped in the northwest part of the Kittitas Valley (Figure 1). In the southern Kittitas Valley, Potato Hill (Figures 2b, 4b, and S2) exposes stratigraphic relationships between the units in a ~10 m deep gravel quarry cut into the side of a prominent, north sloping geomorphic surface (Figure 4b). This outcrop comprises a 1–2 m thick loess mantle over a 2–3 m thick package of weakly cemented Thorp Gravel truncating north dipping beds in the underlying Ellensburg Formation (Figures 4b and 5a). Underlying Ellensburg Formation beds dip up to ~10° to the north, while the surface of Potato Hill and the capping Thorp Gravel have lesser northward slopes of ~3–5°. The angular unconformity between Ellensburg and Thorp bedding is consistent with syntectonic deposition of the Thorp Gravel and indicates progressive northward tilting in the basin north of Manastash Ridge starting before or sometime after the deposition of the Ellensburg Formation [*Bentley*, 1977]. We sampled the base of Thorp Gravel at Potato Hill (Table 1 and Figure S2) to assess a local burial age.

### 4.2. Manastash Ridge

The Manastash Ridge range front forms the southern topographic and structural boundary of the Kittitas Valley (Figures 2a, 2b, and 4a). The Manastash and subsidiary Thrall anticlines (Figures 2a and 2b) developed above southwest dipping range front reverse faults [*Bentley*, 1977; *Ladinsky*, 2012]. We sampled three of the five geomorphically distinct strath terrace levels that occupy the Manastash Ridge reach of the Yakima River Canyon.

On the east side of the Yakima River Canyon entrance, the Manastash Ridge range front preserves the highest (~150 m above the channel) and most extensive strath terrace associated with the canyon. The terrace comprises a thick loess deposit mantling rounded basaltic cobbles that overlie a basalt strath surface, all of which

are exposed as floats on the south flank of the terrace (Figure 2b). We recovered cobbles from this terrace in a ~0.6 m thick deposit of angular to well-rounded pebble to small cobble-sized basalt clasts directly overlying basaltic bedrock strath at the base of a 1.2 m deep backhoe pit in the terrace. The $<$2 m thickness of the deposit and the lack of quartz in the basaltic clasts prevented isochron burial dating of the deposit.

The Yakima River exposes the core of the Manastash anticline in an abandoned meander buried by colluvium, loess, and fan deposits (Figure 2b), where *Ladinsky* [2012] mapped six terrace levels and determined infrared stimulated luminescence (IRSL) ages for loess above one Yakima River terrace gravel deposit. We mapped four strath terrace levels above the floodplain at this location, including sites mapped by *Ladinsky* [2012], and sampled gravels at two of the sites, here termed the Toth Road and Rattlesnake Dance terraces.

The Toth Road site exposes a 4–5 m thick fluvial gravel deposit overlain by fan deposits above the folded Columbia River basalt of the Thrall anticline, 54–58 m above the active channel (Figures 2b, 5b, and S3). Hill slope material conceals the strath at the Toth Road site, so we mapped the strath contact as the upper extent of angular basalt clasts in rounded gravel (Table 1 and Figures 2a and 2b). The Rattlesnake Dance terrace consists of a ~3 m thick gravel deposit (Figures 2a, 2b, and S4) overlain by ~3 m of loess and capping a basalt strath, positioned 19–21 m above the active channel, in the core of the Manastash anticline (Figures 2b and 5c). The Yakima River floodplain surface (Figures 2a and 2b) is roughly 17 m below the Rattlesnake Dance terrace (Figure 5c).

### 4.3. Manastash-Umtanum Syncline

At the site we refer to as Meander Terrace, the Yakima River incises a cutoff meander in the synclinal trough between the Manastash and Umtanum Ridge anticlines (Figures 2c and S5). We mapped three Meander Terrace gravel deposits capping basalt straths at two levels vertically separated by ~10 m (Figures 2a and 2c). The gravels are nearly continuously covered by several meters of loess and basaltic colluvium shed from the steep-abandoned meander walls (Figure 2c). We sampled the lowest gravel deposit at this site directly above the strath and ~2 m below the top of the gravel (Figure S5).

### 4.4. Umtanum Ridge

We sampled at four sites among the four levels of strath terraces that occur where the Yakima River incises across Umtanum Ridge (Figures 2 and 3). The second and third highest sites that we sampled in the canyon are along this reach, near a location locally referred to as the "Wymer Cut" and informally named the Lower and Higher Island terraces (Figures 2c and S6–S9). The Island terraces are on the north limb of Umtanum Ridge near the location of several mapped, north dipping thrust splays (Figures 2a and 2c), and therefore occupy a structural high despite their location several kilometers upstream of the anticlinal axis.

The Higher Island site comprises a 4–5 m thick gravel deposit capping a well-exposed strath positioned ~100 m above the active channel and preserves a broad, intact tread (Figures 2c, 5e, S6, and S9). We sampled the gravel in a hand-dug pit directly (0.0–0.2 m) over the strath, 3–5 m below the deposit tread, but only 1.9 to 1.7 m below the sloping surface of the gravel riser (Figure S9).

The Lower Island terrace is inset ~20–30 below the Higher Island terrace and comprises a $\leq$4 m thick gravel deposit capping a well-exposed basalt strath 60–64 m above the active channel (Figures 2c, 5e, and S6–S8). We sampled the gravel ~1 m above the strath and 2–3 m below the top of the gravel. A highway road cut through the Lower Island terrace exposes the gravel-over-basalt strath relationship, as well 3–4 m of horizontally bedded, white to brown colored sand, silt, and clay overlying the gravel (Figures S7 and S8). This sedimentary package also includes possible paleosols and lacustrine diatomites interfingered with colluvium stringers that pinch out to the south. We speculate that this sediment was deposited over the previously developed strath terrace in a landslide-dammed lake. The entire exposure is uniformly capped by a thick (~50 cm) brown soil that follows the topographic surface.

The site that we informally name Death Chute terrace corresponds with the deepest (~600 m) section of the Yakima River Canyon in the core of the Umtanum Ridge anticline. At this site, a road cut exposes a $\leq$5 m thick gravel deposit capping a well-exposed basalt strath positioned 36–39 m above the active channel (Figures 2a, 2d, 5f, and S10). The basalt strath in this location is strongly fractured (Figure S10), likely related to its location between two exposed thrust faults (Figure 2d). We sampled the gravel directly (0.0–0.2 m) over the strath and ~4 m below the top of the gravel beneath the poorly expressed terrace tread.

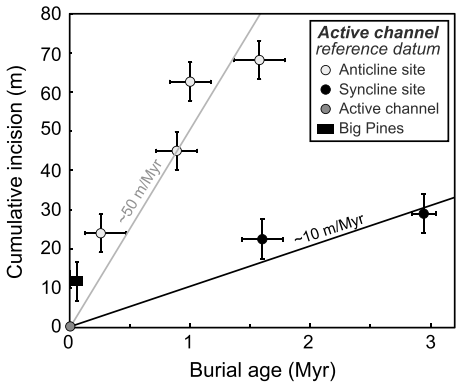


**Figure 6.** Bayesian linear regressions of Yakima River strath terrace age and cumulative bedrock incision across the anticlines and synclines calculated relative to the active bedrock channel. The Big Pines age range and elevation are plotted but not regressed.

The informally named Big Pines terrace represents the geomorphically lowest deposit we sampled, with the terrace tread occurring up to 9 m above the Yakima River near the core of the Umtanum Ridge anticline (Figures 2d, 5g, and S11). The Big Pines terrace comprises a 6 m thick gravel deposit capping a basalt strath positioned ≲3 m above the active channel (Figure 5g) and features a broad intact tread surface mantled by a thin (10–20 cm) rocky light brown soil truncating prominent massive south dipping gravel beds (Figure S11). We sampled the gravel ~2 m above the strath and 4 m below the deposit tread.

## 5. Burial Age and Incision Rate Results

In this section, we report $^{26}$Al-$^{10}$Be isochron burial ages and bedrock incision data summarized in Table 1. The ages are calculated based on cosmogenic isotope data reported in Table S1. Of the 40 samples we analyze to determine burial ages, 10 were collected and measured by *Coppersmith et al*. [2014] (Table S1). We report bedrock incision rates for each site based on the burial ages and cumulative local incision relative to the active bedrock channel. We also report long-term rates of bedrock incision across the anticlines and synclines (Figure 6). We then compare incision rates calculated using the active channel datum with long-term rates referencing the age and elevation of the lowest dated strath as an alternate datum in the accompanying supporting information file (Table S2 and Figure S12) [*Gallen et al*., 2015]. Slope uncertainties reflect the 1$\sigma$ range for sites with Gaussian slope output distributions and the 68% confidence interval for asymmetrical slope outputs. Incision rate uncertainties reflect the nominal bedrock incision uncertainty (5 m) and 1$\sigma$ burial age errors propagated in quadrature for sites with Gaussian posterior slope errors and calculated based on the range of incision rates allowed by the maximum and minimum 68% confidence interval burial ages for sites with asymmetrical posterior slope uncertainties.

### 5.1. Potato Hill, Kittitas Valley

Potato Hill samples ($n = 3$) fit a line (slope = 1.67 ± 0.09, $R^2 = 0.98$) that implies a burial age of 2.9 ± 0.1 Ma for the Thorp Gravel (Figure 3a). Despite being ~0.7 Myr younger, the burial age is consistent with *Waitt*'s [1979] zircon fission track age of 3.64 ± 0.37 (1$\sigma$) Ma of tephra in the Thorp Gravel for several reasons. Potato Hill is ~25–35 km downstream of *Waitt*'s [1979] sample site (Figure 1), hence, a transportation lag time may account for the younger burial age if the outwash deposits mapped as Thorp Gravel prograded to the southeast across Kittitas Valley. Another possibility, given the lack of a continuous geomorphic surface related to the Thorp Gravel between the type location and Potato Hill, is that the local deposits represent temporally discrete facies of the unit. The burial age of the Thorp Gravel and cumulative bedrock incision at Potato Hill (28 ± 5 m) suggest a local bedrock incision rate of 10 ± 2 m/Myr.

### 5.2. Manastash Ridge

Toth Road samples ($n = 5$) yield an isochron (slope = 4.12 ± 0.45, $R^2 = 0.95$) burial age of 1.0 ± 0.2 Ma for the gravel (Figure 3b). The Toth Road gravel burial age and cumulative bedrock incision (62 ± 5 m) indicate a local incision rate of 61 ± 13 m/Myr. Isochron analysis of the Rattlesnake Dance terrace samples ($n = 5$, slope = 6.10 + 0.40/−0.70, $R^2 = 0.91$) implies a burial age of 0.2 + 0.3/−0.1 Ma for the gravel (Figure 3c), older than *Ladinsky*'s [2012] IRSL age of 84.2–93.3 ka for the overlying loess, and overlapping the ~0.2 Ma lower age limit of the isochron burial method [*Balco and Rovey*, 2008]. The Rattlesnake Dance gravel burial age and cumulative bedrock incision (23 ± 5 m) suggest a local bedrock incision rate of 114 + 164/−79 m/Myr. Also, the Rattlesnake Dance terrace is inset 39 ± 7 m lower than the ~1.0 Ma Toth Road terrace (Figure 2b), suggesting an interval incision rate of ~50 m/Myr over the ~0.8 Myr period between the formation of these terraces.

### 5.3. Manastash-Umtanum Syncline

Meander Terrace samples ($n = 5$) have a mode linear fit (slope = 3.27 ± 0.34, $R^2 = 0.89$) that corresponds with a burial age of 1.6 ± 0.2 Ma for the gravel (Figure 3d). Based on the Meander Terrace burial age and cumulative local bedrock incision (22 ± 5 m), bedrock incision across the Manastash-Umtanum syncline occurs at a local rate of 14 ± 4 m/Myr.

### 5.4. Umtanum Ridge

Higher Island terrace samples ($n = 6$) have a narrow range of $^{10}$Be (6.10 to 7.17 × $10^4$ atoms/g) and $^{26}$Al (3.66 to 4.48 × $10^5$ atoms/g) concentrations that prevent interpretation of the isochron analysis results (slope = 6.44 + 0.09/−1.11, $R^2 = 0.67$). We report no burial age for the Higher Island terrace; however, the geomorphically inset Lower Island terrace ($n = 4$, slope = 3.21 ± 0.40, $R^2 = 0.98$) yields an isochron burial age of 1.6 ± 0.3 Ma for the gravel (Figure 3f) that constrains the Higher Island gravel burial age to ≥1.6 Ma. The Lower Island gravel burial age matches the Meander terrace gravel burial age, possibly suggesting contemporaneous deposition and strath terrace formation. The Lower Island terrace burial age and cumulative local bedrock incision (68 ± 5 m) correspond with a bedrock incision rate of 42 ± 9 m/Myr.

Isochron analysis of Death Chute samples ($n = 5$) yields a slope well below the production ratio (slope = 4.30 ± 0.43, $R^2 = 0.84$) and implies a burial age of 0.9 ± 0.2 Ma for the gravel (Figure 3g). The Death Chute gravel burial age and cumulative bedrock incision (44 ± 5 m) suggest a local bedrock incision rate of 49 ± 12 m/Myr.

Big Pines samples overlap the production ratio within uncertainty ($n = 3$, slope = 6.70 + 0.02/−0.24, $R^2 = 0.85$), implying an isochron burial age for the gravel (0.0 + 0.1/−0.0 Ma) that is indistinguishable from modern (Figure 3h). Although the uncertain burial age allows Holocene deposition of the Big Pines gravel deposition, the local bedrock incision rate a few kilometers upstream at the Death Chute terrace (~49 m/Myr, Figure 2d) and 12 ± 5 m of local downcutting is consistent with deposition during the Pleistocene. The uncertain maximum burial age we calculate at Big Pines (0.1 Ma) permits that local bedrock incision may occur at a minimum rate of 66 m/Myr.

### 5.5. Long-Term Average Incision Rates

We assess long-term average rates of bedrock incision for the Yakima River terraces by regressing cumulative bedrock incision against gravel burial age [e.g., *Pederson et al.*, 2006, 2013]. The regression slopes indicate that over the long term, average rates of bedrock incision are roughly 5 times faster across the anticlines (50 m/Myr) than across the synclines (10 m/Myr) (Figure 6). We omit the Big Pines site from the anticline regression because its burial age is indistinguishable from zero.

We consider the undated Big Pines strath as an alternate reference datum for calculating local bedrock incision [*Gallen et al.*, 2015]. Based on the probable Pleistocene deposition and the range of permissible burial ages (0.0 to 0.1 Ma), we assume a finite age and uncertainty of 0.1 ± 0.1 Ma for Big Pines terrace. We subtract the age (0.1 ± 0.1 Myr) and cumulative local bedrock incision (12 ± 5 m) from the higher, older sites to calculate cumulative incision and measurement interval (Table S2) relative to the Big Pines datum. Since the Big Pines terrace is located near the core of the Umtanum Ridge anticline, and we lack a comparable dated Pleistocene strath in either syncline, we limit the alternate datum approach strictly to anticlinal sites where incision rates are likely to be similar (e.g., Figure 6). The regression slope for incision versus measured interval calculated relative to the Big Pines reference datum indicates a long-term average bedrock incision rate (42 ± 4 m/Myr, Figure S12) that nearly matches the long-term active channel-based rate across the anticlines (50 m/Myr, millimeter-scale uncertainty).

Given similarities between long-term bedrock incision rates calculated relative to either datum, it appears unlikely that the incision rates we calculate relative to the active channel are susceptible to measurable bias from the potentially transient active channel elevation [*Gallen et al.*, 2015; *Finnegan et al.*, 2014]. Additionally, the uncertain age of the Big Pines terrace limits the applicability of the alternate datum approach to our data set. We therefore base our neotectonic interpretations on local rates of bedrock incision calculated with respect to the active bedrock channel and the measured burial age at each site.

## 6. Discussion

Several lines of evidence suggest that the distribution of strath terrace gravels and ages in the Yakima River Canyon reflects the spatial pattern of fluvial incision and Quaternary deformation across the Manastash and

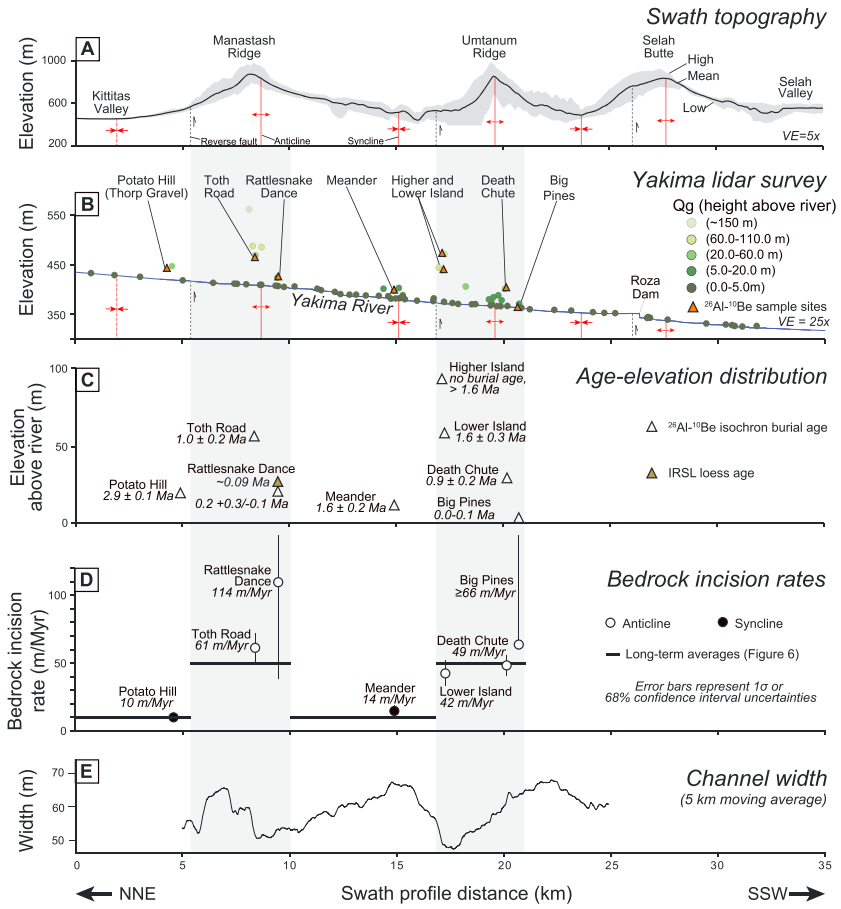


**Figure 7.** Profiles projected to the swath topography profile line (location shown in Figure 2a) comparing topography, structure, terrace location, age, and incision rates with grey bars interpreting correlation between structural highs and other data. (a) 2.5 km wide swath topographic profile (Figure 2a) from the 10 m Washington State DEM. The thick black profile line represents mean elevation, and the grey envelope represents maximum and minimum elevations along the swath in Figure 2a. Structures are projected to line at approximate surface location and represent the primary faults and folds associated with each ridge. (b) Cosmogenic sample sites, mean elevations of mapped strath terrace gravels, Yakima River long profile, and structures projected below the approximate river-surface intersection. (c) Cosmogenic $^{26}$Al-$^{10}$Be isochron burial ages for each site plotted by height above the river (sample elevation minus river elevation) over profile distance. (d) Incision rates calculated from cosmogenic $^{26}$Al-$^{10}$Be isochron burial ages and cumulative incision referencing the active bedrock channel. (e) Yakima River Canyon channel width data [*Coppersmith et al.*, 2014, Appendix E].

Umtanum Ridge folds. Comparing the average topography and bedrock structure along the canyon (Figure 7a) with terrace heights (Figure 7b) and ages (Figure 7c) shows that the Manastash and Umtanum Ridge anticlines preserve substantially more terrace remnants and levels than Kittitas Valley or the intervening syncline (Figures 7a and 7b). The spatial distribution of terrace remnants and associated burial ages likely results from high rates of Quaternary rock uplift in the anticlines (relative to the synclines), such that strath terraces with equivalent burial ages are more rapidly uplifted above the active channel where it crosses the anticlines. For example, the ~1.6 Ma synclinal terrace gravel at Meander terrace is positioned only ~14 m above the active channel, whereas another ~1.6 Ma terrace gravel occurs ~60 m above the channel at the Lower Island terrace in the Umtanum Ridge anticline (Figure 7c).

The distribution of local and long-term average bedrock incision rates is also consistent with differential Quaternary rock uplift across the anticlines. Local bedrock incision across the Manastash (~61 to 114 m/Myr over ~1.0 Myr) and Umtanum Ridge (~42 to 49 m/Myr over ~1.6 Myr) anticlines occurs 4–10 times faster than at sites directly upstream in Kittitas Valley (~10 m/Myr over ~2.9 Myr) and in the intervening syncline (~14 m/Myr over ~1.6 Myr) (Figure 7d). Additionally, we observe that the long-term rate of bedrock incision averaged across the Manastash and Umtanum Ridge anticlines (~50 m/Myr, Figure 6) is roughly a

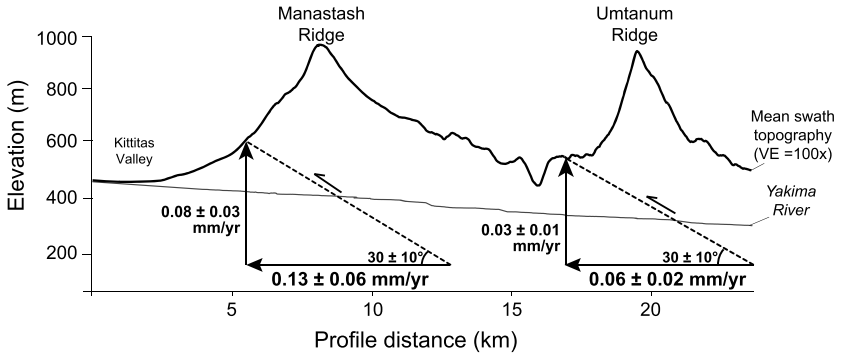


**Figure 8.** Simple model estimating time-averaged shortening rates across south dipping master reverse faults beneath Manastash and Umtanum Ridge folds. The calculation assumes that the average of the local rates of differential bedrock incision across each fold is equal to the corresponding average rates of differential rock uplift (see section 6 for detailed explanation). Topographic profile uses the same data as Figure 7a, and Yakima River profile is the same as in Figure 7b.

factor of 5 higher than the long-term rate averaged across the intervening syncline and the Kittitas Valley upstream (~10 m/Myr, Figure 6). Substantial overlap between local and long-term average bedrock incision rates within the anticlines and synclines (Figure 7d) suggests that the related rates of differential rock uplift across the folds have remained relatively stable over the past ~1.6–2.9 Myr.

To assess the rates of rock uplift that drive differential bedrock incision across the anticlines, we consider the background rate of incision across the synclines. Near the head of the canyon in the Kittitas Valley, the local incision rate at Potato Hill (10 ± 2 m/Myr spanning ~2.9 Myr, Figures 7c and 7d) overlaps the local rate calculated for the synclinal Meander Terrace (14 ± 4 m/Myr spanning ~1.6 Ma, Figures 7c and 7d). The match between the synclinal rates suggests a similar, modest background rate of downcutting and relative base level fall both outside and within the canyon. Therefore, subtracting the similar low synclinal rates from the much higher anticlinal rates of bedrock incision directly estimates the associated rates of ongoing rock uplift. We calculate an average background rate of incision (12 ± 4 m/Myr) based on the local Potato Hill and Meander Terrace incision rates and subtract the background rate from the average of the local incision rates across Manastash (88 ± 32 m/Myr) and Umtanum Ridge (46 ± 8 m/Myr) anticlines. The differences provide average rates of differential bedrock incision and rock uplift resulting from the vertical component of the underlying faulting across the Manastash (76 ± 32 m/Myr) and Umtanum Ridge (34 ± 9 m/Myr) anticlines (Figure 8).

Spatial variations in bedrock incision rate and channel narrowing are also consistent with expectations of fluvial response to differential rock uplift on the Yakima River across the Manastash and Umtanum Ridge structures. Incision rates along the Yakima River Canyon correspond spatially with changes in channel width (Figure 7e). The Yakima River channel maintains relatively constant slope through the canyon (Figure 7b) but narrows across Manastash and Umtanum Ridge anticlines [*Coppersmith et al*., 2014, Appendix E; *Fisher et al*., 2013] near measured high incision rates and the exposed reverse fault at the mouth of the canyon (Figures 7a–7e). The channel narrowing occurs over wavelengths that are relatively short in comparison to the anticlines and colocated zones of relatively high incision and rock uplift rates (Figure 7e). The zones of channel narrowing do not, however, correspond to large debris flows or other point sources of coarse sediment in the canyon. Several studies demonstrate that channel width changes can occur across zones of active differential uplift without concomitant channel steepening or preservation of knickpoints [e.g., *Lavé and Avouac*, 2001; *Amos and Burbank*, 2007; *Allen et al*., 2013]. Based on the spatial overlap between modern channel narrowing and relatively high differential bedrock incision rates over ~1–2 Myr, we infer that both the Yakima River channel geometry and the spatial incision rate distribution represent long-term features of Yakima River channel response to ongoing folding, faulting, and related rock uplift.

It remains unclear whether faulting or folding primarily drives differential rock uplift across the Yakima folds. Deformed terraces have been used to infer the geometries and kinematics of fault-related folds in a variety of climatic and tectonic settings [e.g., *Lavé and Avouac*, 2001; *Amos et al*., 2007]. Such inferences require intact and relatively continuous terrace treads, unlike the relatively sparse and discontinuous terrace treads preserved in the Yakima River Canyon. Thus limited, we instead explore the deformation rates implied by our

incision rate data using a simple geometric model of folding and rock uplift across the Yakima folds controlled by slip on underlying thrust faults (Figure 8) [e.g., *Blakely et al*., 2011; *Reidel*, 1984; *West et al*., 1996]. Our model is general enough to be consistent with either the fault-propagation [*Suppe and Medwedeff*, 1990] or fault-bend model [*Casale and Pratt*, 2015; *Suppe*, 1983].

We relate the local average differential rock uplift rates across the Manastash (0.08 ± 0.03 mm/yr) and Umtanum Ridge (0.03 ± 0.01 mm/yr) anticlines to rates of shortening associated with reverse slip on master fault planes underlying each fold (Figure 8). We compute hypothetical shortening rates (Figure 8) based on the geometric relationship between rock uplift rate and master faults dipping ~30° south [*Ladinsky*, 2012; *Miller*, 2014], adding a representative fault dip uncertainty of 10°. This approach estimates horizontal shortening spanning the $10^6$ year measurement interval at rates of 0.13 ± 0.06 mm/yr and 0.06 ± 0.02 mm/yr on faults beneath the Manastash and Umtanum Ridge anticlines, respectively.

Although the modern, geodetically inferred shortening integrates ~20 years of measurement, the implied rate and orientation matches the 16 Myr geologic record of deformation along the Cascadia convergent margin [*Wells et al*., 1998; *Wells and McCaffrey*, 2013]. Close agreement between the deformation records spanning $10^1$ to $10^7$ years permits extrapolation of the regional geodetic rates over the $10^6$ year measurement interval of the Manastash and Umtanum Ridge shortening rates that we report [*Wells and McCaffrey*, 2013]. The combined shortening rate we calculate for Manastash and Umtanum Ridge folds spanning the past ~1.1–1.6 Myr (~0.2 mm/yr) accounts for a relatively small fraction (~10%) of the modern regional shortening (1.9 ± 0.5 mm/yr) [*McCaffrey et al*., 2013], suggesting that long-term deformation on other Yakima folds and faults has occurred at equivalent or slightly faster rates. Alternatively, the point estimates of shortening that we report may not reflect the average rate spanning the length of the structures, in which case other segments of the folds may take up more or less shortening.

Given the comparative absence of data on Yakima folds and faults other than Manastash and Umtanum, it remains unclear which structures take up the remaining active shortening. Between the geodetic rate and the rates that we report, however, it is clear that the Manastash and Umtanum Ridge anticlines are actively deforming at modest rates. Consequently, reverse faults driving deformation across the anticlines may pose a seismic hazard, particularly given the $M_w > 7$ seismic potential of the apparent ~200 km cumulative length of the related faults [*Blakely et al*., 2011; *Wells and Coppersmith*, 1994]. The relative lack of information about the remaining potentially active structures, which include 12 fault-related folds [e.g., *Reidel*, 1984] and a number of right-lateral strike-slip faults [*Anderson et al*., 2013], results in considerable uncertainty surrounding the seismic hazard of individual structures within the Yakima folds.

Bedrock incision rates also help constrain the age of the Yakima River Canyon (Figure 2). We extrapolate the time-averaged rate of downcutting through the approximate pre-erosion relief of the structural topographic high at the Umtanum Ridge anticline to consider the timespan necessary to cut the maximum canyon depth. *Miller*'s [2014] structural cross section places the crest of the Umtanum Ridge anticline, developed in ~15.7 Ma Grand Ronde basalt, roughly 640 m above the modern Yakima River channel. Incising this depth at the average local rate of ~46 m/Myr requires ~14 Myr. This estimated age of the Yakima River Canyon inception suggests that incision and folding of the oldest rocks likely began soon after the time of their emplacement.

## 7. Conclusions

We mapped and dated strath terraces in the Yakima River Canyon and calculated bedrock incision rates spanning Manastash and Umtanum Ridge structures. Bayesian regression and cosmogenic $^{26}$Al-$^{10}$Be isochron analysis provided burial ages of Cascade-derived, strath-capping gravels in the Yakima River Canyon and the Kittitas Valley, characterizing intervals of terrace formation and incision spanning the past ~2.9 Myr. In combination with our mapping, analysis of the lidar data indicates that strath elevations range up to ~150 m above the active channel with the highest strath terraces occurring in the anticlines and lower terraces within synclines. Average bedrock incision rates derived from $^{26}$Al-$^{10}$Be isochron burial ages, lidar elevations, and well log data are 4 to 8 times higher across Manastash (~88 m/Myr) and Umtanum Ridge (~46 m/Myr) anticlines than in the Manastash-Umtanum syncline and the Kittitas Valley (~12 m/Myr). Extrapolating the average Umtanum Ridge anticline incision rate over the maximum canyon depth suggests that the Yakima River Canyon has been a feature of the landscape since well before Quaternary time.

Collectively, the results are consistent with steady average rates of differential bedrock incision and uplift throughout the Quaternary. We use the differential rock uplift rates (Manastash ≈ 0.08 mm/yr, Umtanum ≈ 0.03 mm/yr) to estimate horizontal shortening across the Manastash (~0.13 mm/yr) and Umtanum Ridge (~0.06 mm/yr) anticlines based on the assumption that both folds verge in the direction of the associated reverse faulting at depth (dip 30 ± 10° south). These estimates suggest that the two folds take up ~10% of the contemporary geodetic shortening rate (1.9 ± 0.5 mm/yr) [*McCaffrey et al*., 2013]. It remains unclear which of the other Yakima folds and faults actively accommodate the remaining geodetic strain, highlighting the need for further geologic investigations of the tectonic structures and associated seismic hazard across central Washington.

**Acknowledgments**

This research was supported by the U.S. Geological Survey (USGS), Department of the Interior, under USGS National Earthquake Hazard Reduction Program award number (C. Amos, G14AP00050), (P. Bierman, G14AP00054), and (D. Rood, G14AP00055), as well as graduate student research grants from the Geological Society of America and Western Washington University awarded to A. Bender. The USGS Earthquake Hazards Project supported A. Bender during final revisions of this manuscript. Base hillshade and topographic maps for Figures 1 and 2 were derived from Washington 10 m DEM (http://gis.ess.washington.edu/data/raster/tenmeter/byquad/). Fault linework and bedrock geology used in Figures 1 and 2 were available at (http://www.dnr.wa.gov/ResearchScience/Topics/GeosciencesData/Pages/gis_data.aspx). The lidar data set used in this study is freely available through the OpenTopography web portal (doi:10.5069/G9KW5CXQ). Supporting cosmogenic geochemistry data are included in the supporting information Table S1. The MATLAB scripts and input files necessary to recreate the isochrons in this paper are available from the corresponding author on request (abender@usgs.gov). Channel width data are generated by S. Sorsby and available online in Appendix E supporting information (part I) at http://www.hanford.gov/page.cfm/OfficialDocuments/HSPSHA. We are grateful to G. DeLuca and O. Mayer for their hospitality; Z. DeLuca, M. Holland, and K. Frank for their help in the field; and V. Sosa-Gonzales, L. Corbett, T. Neilson, and B. DeJong for their guidance in the lab. We thank landowners in the Yakima River canyon for granting access to their property. This manuscript benefitted from constructive reviews by L. Schermer, J. O'Connor, S.E.K. Bennett, K. Wegmann, and one anonymous reviewer. Any use of trade, product, or firm names is for descriptive purposes only and does not imply endorsement by the U.S. Government.

## References

Allen, G. H., J. B. Barnes, T. M. Pavelsky, and E. Kirby (2013), Lithologic and tectonic controls on bedrock channel form at the northwest Himalayan front, *J. Geophys. Res. Earth Surf.*, *118*, 1806–1825, doi:10.1002/jgrf.20113.

Amos, C. B., and D. W. Burbank (2007), Channel width response to differential uplift, *J Geophys Res*, *112*, F02010, doi:10.1029/2006JF000672.

Amos, C. B., D. W. Burbank, D. C. Nobes, and S. A. L. Read (2007), Geomorphic constraints on listric thrust faulting: Implications for active deformation in the Mackenzie Basin, South Island, New Zealand, *J. Geophys. Res.*, *112*, B03S11, doi:10.1029/2006JB004291.

Anderson, J. L., T. L. Tolan, and R. E. Wells (2013), Strike-slip faults in the western Columbia River flood basalt province, Oregon and Washington, *Geol. Soc. Am. Spec. Pap.*, *497*, 325–347, doi:10.1130/2013.2497(13).

Argento, D., R. Reedy, and J. Stone (2013), Modeling the Earth's cosmic radiation, *Nucl. Instrum. Methods Phys. Res. B*, *294*, 464–469, doi:10.1016/j.nimb.2012.05.022.

Balco, G., and C. W. Rovey (2008), An isochron method for cosmogenic-nuclide dating of buried soils and sediments, *Am. J. Sci.*, *308*(10), 1083–1114, doi:10.2475/10.2008.02.

Bentley, R. D. (1977), Stratigraphy of the Yakima basalts and structural evolution of the Yakima ridges in the western Columbia Plateau, in *Geological Excursions in the Pacific Northwest*, edited by E. H. Brown and R. C. Ellis, Western Washington Univ. Press, Washington Published as a geology field guide in conjunction with the 1977 annual meeting of the Geol. Soc. Am., p. 51.

Bingham, J. W., and M. J. Grolier (1966), The Yakima basalt and Ellensburg formation of south-central Washington, U.S. Geol. Surv. Bull. 1224–B. [Available at http://pubs.usgs.gov/bul/1224g/report.pdf.]

Blakely, R. J., R. E. Wells, C. S. Weaver, and S. Y. Johnson (2002), Location, structure, and seismicity of the Seattle fault zone, Washington: Evidence from aeromagnetic anomalies, geologic mapping, and seismic-reflection data, *Geol. Soc. Am. Bull.*, *114*(2), 169–177, doi:10.1130/0016-7606(2002)114<0169:LSASOT>2.0.CO;2.

Blakely, R. J., B. L. Sherrod, C. S. Weaver, R. E. Wells, A. C. Rohay, E. A. Barnett, and N. E. Knepprath (2011), Connecting the Yakima fold and thrust belt to active faults in the Puget Lowland, Washington, *J. Geophys. Res.*, *116*, B07105, doi:10.1029/2010JB008091.

Blakely, R. J., B. L. Sherrod, C. S. Weaver, A. C. Rohay, and R. E. Wells (2012), Tectonic setting of the wooded island earthquake swarm: Eastern Washington, *Bull. Seismol. Soc. Am.*, *102*(4), 1786–1795, doi:10.1785/0120110189.

Blakely, R. J., B. L. Sherrod, C. S. Weaver, R. E. Wells, and A. C. Rohay (2014), The Wallula fault and tectonic framework of south-central Washington, as interpreted from magnetic and gravity anomalies, *Tectonophysics*, *624*, 32–45, doi:10.1016/j.tecto.2013.11.006.

Borchers, B., S. Marrero, G. Balco, M. Caffee, B. Goehring, N. Lifton, K. Nishiizumi, F. Phillips, J. Schaefer, and J. Stone (2015), Geological calibration of spallation production rates in the CRONUS-Earth project, *Quat. Geochronol.*, doi:10.1016/j.quageo.2015.01.009.

Bretz, J. H. (1969), The Lake Missoula floods and the channeled scabland, *J. Geol.*, *505*, –543, doi:10.1086/627452.

Bull, W. B. (1991), *Geomorphic Responses to Climatic Change*, 326 pp., Oxford Univ. Press, New York.

Burbank, D. W., and Anderson, R. S. (2011), *Tectonic Geomorphology*, John Wiley, Chichester, U. K., doi:10.1002/9781444345063.

Campbell, N. P., and R. D. Bentley (1981), Late Quaternary deformation of the Toppenish Ridge uplift in south-central Washington, *Geology*, *9*(11), 519, doi:10.1130/0091-7613(1981)9<519:LQDOTT>2.0.CO;2.

Casale, G., and T. L. Pratt (2015), Thin- or thick-skinned faulting in the Yakima fold and thrust belt (WA)? Constraints from kinematic modeling of the Saddle Mountains anticline, *Bull. Seismol. Soc. Am.*, doi:10.1785/0120140050.

Chmeleff, J., F. von Blanckenburg, K. Kossert, and D. Jakob (2010), Determination of the $^{10}$Be half-life by multicollector ICP-MS and liquid scintillation counting, *Nucl. Instrum. Methods Phys. Res. B*, *268*(2), 192–199, doi:10.1016/j.nimb.2009.09.012.

Çiner, A., U. Doğan, C. Yıldırım, N. Akçar, S. Ivy-Ochs, V. Alfimov, P. W. Kubik, and C. Schlüchter (2015), Quaternary uplift rates of the Central Anatolian Plateau Turkey: Insights from cosmogenic isochron-burial nuclide dating of the Kızılırmak River terraces, *Quat. Sci. Rev.*, *107*, 81–97, doi:10.1016/j.quascirev.2014.10.007.

Coppersmith, K. J., et al. (2014), Hanford sitewide probabilistic seismic hazard analysis, PNNL-23361, Pacific Northwest National Laboratory, Richland, Wash. [Available at http://www.hanford.gov/page.cfm/OfficialDocuments/HSPSHA.]

Corbett, L. B., N. E. Young, P. R. Bierman, J. P. Briner, T. A. Neumann, D. H. Rood, and J. A. Graly (2011), Paired bedrock and boulder $^{10}$Be concentrations resulting from early Holocene ice retreat near Jakobshavn Isfjord, western Greenland, *Quat. Sci. Rev.*, *30*(13), 1739–1749, doi:10.1016/j.quascirev.2011.04.001.

D'Agostini, G. (2003), Bayesian reasoning in data analysis, *World Sci.*, doi:10.1142/5262.

D'Agostini, G. (2005), Fits, and especially linear fits, with errors on both axes, extra variance of the data points and other complications, arXiv preprint physics/0511182.

Darling, A. L., K. E. Karlstrom, D. E. Granger, A. Aslan, E. Kirby, W. B. Ouimet, G. D. Lazear, D. D. Coblentz, and R. D. Cole (2014), New incision rates along the Colorado River system based on cosmogenic burial dating of terraces: Implications for regional controls on Quaternary incision, *Geosphere*, GES00724-1, doi:10.1130/GES00724.1.

Duvall, A., E. Kirby, and D. Burbank (2004), Tectonic and lithologic controls on bedrock channel profiles and processes in coastal California, *J Geophys Res*, *109*, F03002, doi:10.1029/2003JF000086.

Erlanger, E. D., D. E. Granger, and R. J. Gibbon (2012), Rock uplift rates in South Africa from isochron burial dating of fluvial and marine terraces, *Geology*, *40*(11), 1019–1022, doi:10.1130/G33172.1.

Finnegan, N. J., R. Schumer, and S. Finnegan (2014), A signature of transience in bedrock river incision rates over timescales of 104–107 years, *Nature*, *505*(7483), 391–394, doi:10.1038/nature12913.

Fisher, G. B., B. Bookhagen, and C. B. Amos (2013), Channel planform geometry and slopes from freely available high-spatial resolution imagery and DEM fusion: Implications for channel width scalings, erosion proxies, and fluvial signatures in tectonically active landscapes, *Geomorphology*, *194*, 46–56, doi:10.1016/j.geomorph.2013.04.011.

Gallen, S. F., F. J. Pazzaglia, K. W. Wegmann, J. L. Pederson, and T. W. Gardner (2015), The dynamic reference frame of rivers and apparent transience in incision rates, *Geology*, *43*, 623–626, doi:10.1130/G36692.1.

Gomberg, J., B. Sherrod, M. Trautman, E. Burns, and D. Snyder (2012), Contemporary seismicity in and around the Yakima fold-and-thrust belt in Eastern Washington, *Bull. Seismol. Soc. Am.*, *102*(1), 309–320, doi:10.1785/0120110065.

Granger, D. E. (2006), A review of burial dating methods using $^{26}$Al and $^{10}$Be, *Geol. Soc. Am. Spec. Pap.*, *415*, 1–16, doi:10.1130/2006.2415(01).

Hancock, G. S., and R. S. Anderson (2002), Numerical modeling of fluvial strath-terrace formation in response to oscillating climate, *Geol Soc Am Bull*, *114*(9), 1131–1142, doi:10.1130/0016-7606(2002)114<1131:NMOFST>2.0.CO;2.

Hooper, P. R., and R. M. Conrey (1989), A model for the tectonic setting of the Columbia River basalt eruptions, *Geol. Soc. Am. Spec. Pap.*, *239*, 293–306.

Johnson, S. Y., C. J. Potter, J. J. Miller, J. M. Armentrout, C. Finn, and C. S. Weaver (1996), The southern Whidbey Island fault: An active structure in the Puget Lowland, Washington, *Geol. Soc. Am. Bull.*, *108*(3), 334–354, doi:10.1130/0016-7606(1996)108<0334:TSWIFA>2.3.CO;2.

Johnson, S. Y., S. V. Dadisman, J. R. Childs, and W. D. Stanley (1999), Active tectonics of the Seattle fault and central Puget Sound, Washington—Implications for earthquake hazards, *Geol. Soc. Am. Bull.*, *111*(7), 1042–1053, doi:10.1130/0016-7606(1999)111<1042:ATOTSF>2.3.CO;2.

Kelsey, H. M., B. L. Sherrod, A. R. Nelson, and T. M. Brocher (2008), Earthquakes generated from bedding plane-parallel reverse faults above an active wedge thrust, Seattle fault zone, *Geol. Soc. Am. Bull.*, *120*(11–12), 1581–1597, doi:10.1130/B26282.1.

Kelsey, H. M., B. L. Sherrod, R. J. Blakely, and R. A. Haugerud (2012), Holocene faulting in the Bellingham forearc basin: Upper-plate deformation at the northern end of the Cascadia subduction zone, *J. Geophys. Res.*, *117*, B03409, doi:10.1029/2011JB008816.

Ladinsky, T. C. (2012), Late Quaternary evolution of the Manastash anticline and Manastash range front, Yakima fold belt, Washington: Influence of tectonics and climate [MS Thesis], Humboldt State Univ., 95 pp. [Available at http://hdl.handle.net/2148/1251.]

Lavé, J., and J. P. Avouac (2001), Fluvial incision and tectonic uplift across the Himalayas of central Nepal, *J. Geophys. Res.*, *106*, 26,561–26,591, doi:10.1029/2001JB000359.

Lifton, N., T. Sato, and T. J. Dunai (2014), Scaling in situ cosmogenic nuclide production rates using analytical approximations to atmospheric cosmic-ray fluxes, *Earth Planet. Sci. Lett.*, *386*, 149–160, doi:10.1016/j.epsl.2013.10.052.

Lifton, N., et al. (2015), In situ cosmogenic nuclide production rate calibration for the CRONUS-Earth project from Lake Bonneville, Utah, shoreline features, *Quat. Geochronol.*, *26*, 56–69, doi:10.1016/j.quageo.2014.11.002.

McCaffrey, R., R. W. King, S. J. Payne, and M. Lancaster (2013), Active tectonics of northwestern U.S. inferred from GPS-derived surface velocities, *J. Geophys. Res. Solid Earth*, *118*, 709–723, doi:10.1029/2012JB009473.

Miller, B. A. (2014), On the origin of Umtanum Ridge: Kinematics of Neogene slip, MS thesis, Univ. of Washington. [Available at http://hdl.handle.net/1773/25333.]

Muzikar, P. (2011), Geological constraints and $^{26}$Al–$^{10}$Be burial dating isochrons, *Earth Surf. Processes Landforms*, *36*(7), 946–952, doi:10.1002/esp.2124.

Nelson, A. R., S. Y. Johnson, H. M. Kelsey, R. E. Wells, B. L. Sherrod, S. K. Pezzopane, L.-A. Bradley, R. D. Koehler, and R. C. Bucknam (2003), Late Holocene earthquakes on the Toe Jam Hill fault, Seattle fault zone, Bainbridge Island, Washington, *Geol. Soc. Am. Bull.*, *115*(11), 1388–1403, doi:10.1130/B25262.1.

Nishiizumi, K. (2004), Preparation of $^{26}$Al AMS standards, *Nucl. Instrum. Methods Phys. Res. B*, *223*, 388–392, doi:10.1016/j.nimb.2004.04.075.

Nishiizumi, K., M. Imamura, M. W. Caffee, J. R. Southon, R. C. Finkel, and J. McAninch (2007), Absolute calibration of $^{10}$Be AMS standards, *Nucl. Instrum. Methods Phys. Res. B*, *258*(2), 403–413, doi:10.1016/j.nimb.2007.01.297.

Pazzaglia, F. J., and M. T. Brandon (2001), A fluvial record of long-term steady-state uplift and erosion across the Cascadia forearc high, western Washington State, *Am. J. Sci.*, *301*(4–5), 385–431, doi:10.2475/ajs.301.4-5.385.

Pederson, J. L., M. D. Anders, T. M. Rittenhour, W. D. Sharp, J. C. Gosse, and K. E. Karlstrom (2006), Using fill terraces to understand incision rates and evolution of the Colorado River in eastern Grand Canyon, Arizona, *J. Geophys. Res.*, *111*, F02003, doi:10.1029/2004JF000201.

Pederson, J. L., W. S. Cragun, A. J. Hidy, T. M. Rittenour, and J. C. Gosse (2013), Colorado River chronostratigraphy at Lee's Ferry, Arizona, and the Colorado Plateau bull's-eye of incision, *Geology*, *41*(4), 427–430, doi:10.1130/G34051.1.

Petersen, M. D., et al. (2014), Documentation for the 2014 update of the United States national seismic hazard maps, U.S. Geol. Surv. Open File Rep., 2014–1091, doi:10.3133/ofr20141091.

Porter, S. C. (1976), Pleistocene glaciation in the southern part of the North Cascade Range, Washington, *Geol. Soc. Am. Bull.*, *87*(1), 61, doi:10.1130/0016-7606(1976)87<61:PGITSP>2.0.CO;2.

Pratt, T. L. (2012), Large-scale splay faults on a strike-slip fault system: The Yakima folds, Washington State, *Geochem. Geophys. Geosyst.*, *13*, Q11004, doi:10.1029/2012GC004405.

Raisz, E. (1945), The Olympic-Wallowa Lineament, Abstracts of Proc. Sess., no. 1364, pp. 42–43.

Reidel, S. P. (1984), The Saddle Mountains: The evolution of an anticline in the Yakima fold belt, *Am J Sci*, *284*(8), 942–978, doi:10.2475/ajs.284.8.942.

Reidel, S. P., V. E. Camp, T. L. Tolan, J. D. Kauffman, and D. L. Garwood (2013), Tectonic evolution of the Columbia River flood basalt province, *Geol. Soc. Am. Spec. Pap.*, *497*, 293–324, doi:10.1130/2013.2497(12).

Russell, I. C. (1893), A geological reconnaissance in Central Washington, U.S. Geol. Surv. Bull. 108. [Available at http://pubs.er.usgs.gov/publication/b108.]

Saltus, R. W. (1993), Upper-crustal structure beneath the Columbia River Basalt Group Washington: Gravity interpretation controlled by borehole and seismic studies, *Geol. Soc. Am. Bull.*, *105*(9), 1247–1259, doi:10.1130/0016-7606(1993)105<1247:UCSBTC>2.3.CO;2.

Schuster, J. E. (1994), Geologic map of the east half of the Yakima 1: 100,000 quadrangle, Washington, Washington Division of Geology and Earth Resour.

Sherrod, B. L., T. M. Brocher, C. S. Weaver, R. C. Bucknam, R. J. Blakely, H. M. Kelsey, A. R. Nelson, and R. Haugerud (2004), Holocene fault scarps near Tacoma, Washington, USA, *Geology*, *32*(1), 9–12, doi:10.1130/G19914.1.

Sherrod, B. L., R. J. Blakely, C. S. Weaver, H. M. Kelsey, E. Barnett, L. Liberty, K. L. Meagher, and K. Pape (2008), Finding concealed active faults: Extending the southern Whidbey Island fault across the Puget Lowland, Washington, *J. Geophys. Res.*, *113*, B05313, doi:10.1029/2007JB005060.

Sherrod, B. L., E. Barnett, E. Schermer, H. M. Kelsey, J. Hughes, F. F. Foit, C. S. Weaver, R. Haugerud, and T. Hyatt (2013), Holocene tectonics and fault reactivation in the foothills of the north Cascade Mountains, Washington, *Geosphere*, GES00880-1, doi:10.1130/GES01067.1.

Smith, G. O. (1903), Anticlinal mountain ridges in central Washington, *J. Geol.*, *11*(2), 166–177, doi:10.1086/621067.

Suppe, J. (1983), Geometry and kinematics of fault-bend folding, *Am. J. Sci.*, 684–721, doi:10.2475/ajs.283.7.684.

Suppe, J., and Medwedeff, D. A. (1990), Geometry and kinematics of fault-propagation folding, *Eclogae Geol Helv*, *83*(3), 409–454. [Available at www.researchgate.net/profile/John_Suppe/publication/237044033_Geometry_and_kinematics_of_faultpropagation_folding/links/0c96052536329176ab000000.pdf.]

Waitt, R. B., Jr. (1979), Late Cenozoic deposits, landforms, stratigraphy, and tectonism in Kittitas Valley, U.S. Geol. Surv., Wash. [Available at http://pubs.usgs.gov/pp/1127/report.pdf.]

Waitt, R. B. (1980), About forty last-glacial Lake Missoula jökulhlaups through southern Washington, *J. Geol.*, 653–679, doi:10.1086/628553.

Waitt, R. B. (1985), Case for periodic, colossal jökulhlaups from Pleistocene glacial Lake Missoula, *Geol. Soc. Am. Bull.*, *96*(10), 1271–1286, doi:10.1130/0016-7606(1985)96<1271:CFPCJF>2.0.CO;2.

Walsh, T. J. (1986), Geologic map of the west half of the Toppenish quadrangle, Washington: Washington Division of Geology and Earth Resour. Open File Rep., 86–3.

Watters, T. R. (1988), Wrinkle ridge assemblages on the terrestrial planets, *J. Geophys. Res.*, *93*(B9), 10,236–10,254, doi:10.1029/JB093iB09p10236.

Watters, T. R. (1989), Periodically spaced anticlines of the Columbia plateau, *Geol. Soc. Am. Spec. Pap.*, *239*, 283–292, doi:10.1130/SPE239-p283.

Wegmann, K. W., and F. J. Pazzaglia (2002), Holocene strath terraces, climate change, and active tectonics: The Clearwater River basin, Olympic Peninsula, Washington State, *Geol. Soc. Am. Bull.*, *114*(6), 731–744, doi:10.1130/0016-7606(2002)114<0731:HSTCCA>2.0.CO;2.

Wegmann, K. W., and F. J. Pazzaglia (2009), Late Quaternary fluvial terraces of the Romagna and Marche Apennines, Italy: Climatic, lithologic, and tectonic controls on terrace genesis in an active orogen, *Quat. Sci. Rev.*, *28*(1), 137–165, doi:10.1016/j.quascirev.2008.10.006.

Wells, D. L., and K. J. Coppersmith (1994), New empirical relationships among magnitude, rupture length, rupture width, rupture area, and surface displacement, *Bull. Seismol. Soc. Am.*, *84*(4), 974–1002.

Wells, R. E., and R. McCaffrey (2013), Steady rotation of the Cascade arc, *Geology*, *41*(9), 1027–1030, doi:10.1130/G34514.1.

Wells, R. E., C. S. Weaver, and R. J. Blakely (1998), Fore-arc migration in Cascadia and its neotectonic significance, *Geology*, *26*(8), 759, doi:10.1130/0091-7613(1998)026<0759:FAMICA>2.3.CO;2.

West, M. W., F. X. Ashland, A. J. Busacca, G. W. Berger, and M. E. Shaffer (1996), Late Quaternary deformation, Saddle Mountains anticline, south-central Washington, *Geology*, *24*(12), 1123, doi:10.1130/0091-7613(1996)024<1123:LQDSMA>2.3.CO;2.

Wicks, C., W. Thelen, C. Weaver, J. Gomberg, A. Rohay, and P. Bodin (2011), InSAR observations of aseismic slip associated with an earthquake swarm in the Columbia River flood basalts, *J. Geophys. Res.*, *116*, B12304, doi:10.1029/2011JB008433.

Xu, S., S. P. H. T. Freeman, D. H. Rood, and R. M. Shanks (2015), Decadal $^{10}$Be, $^{26}$Al and $^{36}$Cl QA measurements on the SUERC accelerator mass spectrometer, *Nucl. Instrum. Methods Phys. Res. B*, doi:10.1016/j.nimb.2015.03.064.

York, D. (1966), Least-squares fitting of a straight line, *Can. J. Geophys.*, *44*(5), 1079–1086, doi:10.1139/p66-090.